AGU ADVANCING EARTH AND SPACE SCIENCE

Water Resources Research

RESEARCH ARTICLE
10.1029/2019WR026930

Key Points:

- We propose a novel method of mapping root zone soil moisture noninvasively by ground-penetrating radar
- This method reconstructs 2D/3D distributions of soil moisture by combining the identification of root's signals and spatial interpolation
- Soil moisture distributions noninvasively mapped by the proposed method matched reasonably those obtained by augering

Supporting Information:

- Supporting Information S1

Correspondence to:
L. Guo,
lug163@psu.edu;
guolistory@gmail.com

Citation:
Liu, X., Chen, J., Butnor, J. R., Qin, G., Cui, X., Fan, B., et al. (2020). Noninvasive 2D and 3D mapping of root zone soil moisture through the detection of coarse roots with ground-penetrating radar. *Water Resources Research*, *56*, e2019WR026930. https://doi.org/10.1029/2019WR026930

Received 11 DEC 2019
Accepted 18 APR 2020
Accepted article online 22 APR 2020

Noninvasive 2D and 3D Mapping of Root Zone Soil Moisture Through the Detection of Coarse Roots With Ground-Penetrating Radar

X. Liu[1,2,3], J. Chen[2], J. R. Butnor[4], G. Qin[1], X. Cui[2], B. Fan[1], H. Lin[3], and L. Guo[1,3]

[1]State Key Laboratory of Hydraulics and Mountain River Engineering, College of Water Resource and Hydropower, Sichuan University, Chengdu, China, [2]State Key Laboratory of Earth Surface Processes and Resource Ecology, Faculty of Geographical Science, Beijing Normal University, Beijing, China, [3]Department of Ecosystem Science and Management, The Pennsylvania State University, University Park, PA, USA, [4]USDA Forest Service, Southern Research Station, 81 Carrigan Drive, Aiken Center, University of Vermont, Burlington, VT, USA

Abstract Root zone soil moisture (RZSM) is important in sustaining terrestrial ecosystems and water cycling. However, noninvasive mapping of RZSM remains challenging in the field, especially its spatial variability at local scales. We propose a novel method of applying ground-penetrating radar (GPR) for noninvasive determination of RZSM. First, this method identified coarse root reflections in GPR images to obtain the reflected wave velocity and soil water storage at various locations. Then, the horizontal distributions of soil water storage to different depths were reconstructed using the inverse distance weighted interpolation. The difference in soil water storage between two depths was converted into 2D RZSM distribution for a specific depth interval. Finally, 2D RZSM distributions from a range of depths were combined to produce a 3D visualization of RZSM. The proposed method was validated in two field plots (30 m by 30 m) in shrublands. The comparisons with 2D RZSM distributions from soil cores sampled at 0.2-m depth intervals suggested a reasonable correspondence in both spatial patterns and absolute values, with the average root-mean-square error less than 0.017 $m^3 \cdot m^{-3}$ and correlation coefficients ranging from 0.502 to 0.798 in both plots. Furthermore, 3D visualizations of RZSM were generated based on GPR estimates to demonstrate the spatial variability of soil moisture at the study scale. The proposed method enhances noninvasive characterization of soil moisture down to the root zone, which contributes to a better understanding of the local-scale variability of soil moisture in the subsoil as well as the ecohydrological processes in the soil-plant-atmosphere continuum.

1. Introduction

Root zone soil moisture (RZSM) is an important component of water cycling through the Critical Zone (Cho et al., 2015; Guo & Lin, 2016; Seneviratne et al., 2010). It influences a variety of Critical Zone processes, including the rates of plant transpiration, photosynthesis, and root water uptake. It also affects biogeochemical cycles (Collins & Bras, 2007; Daly et al., 2004; Jonard et al., 2011; Sonkar et al., 2019), plant-soil moisture relations (Asbjornsen et al., 2011; He et al., 2019), and energy and water balances at the land surface (Huang et al., 2017), along with many other land-atmosphere interactions (Ford et al., 2014; Vereecken et al., 2014). In addition, it informs agricultural water management, such as suitable irrigation schemes (Polak & Wallach, 2001). A detailed grasp of the spatial distribution of RZSM is not only key to a better understanding of the complex plant-soil-water interactions (Collins & Bras, 2007; Vereecken et al., 2008) but also improving the hydrological and meteorological models (Babaeian et al., 2019; Das et al., 2008) that provide the foundation for practical recommendations for agricultural and ecosystem management.

Despite advances in field measurements of RZSM at the point scale via soil moisture sensors (e.g., Guo & Lin, 2018; Raffelli et al., 2017; Robinson et al., 2008) and at the regional or continental scales via satellite remote sensing (e.g., the Soil Moisture Active Passive mission; Das et al., 2018), reliable mapping of RZSM at the intermediate scale (e.g., plot or hillslope scales) remains challenging, especially in a noninvasive and repeatable way (Babaeian et al., 2019; Baldwin et al., 2017). Point-based measurements are often laborious and destructive to the soil environment (Liu, Cui, et al., 2019), and satellite remote sensing only measures the top few centimeters of the soil (Li, Tang, et al., 2013). In addition, the limited measured volume of a buried soil moisture sensor and the coarse resolution of satellite data limit their application in depicting the spatial variability of soil moisture at the intermediate scale (Peng et al., 2017; Petropoulos et al., 2013).

Near-surface geophysical methods, such as ground-penetrating radar (GPR), electromagnetic induction (EMI), and electrical resistivity tomography (ERT), have opened new possibilities for intermediate-scale RZSM data collection (Huisman et al., 2002; Robinson et al., 2008). These tools bridge the gaps between point-based measurements and large-scale remote sensing of soil moisture (Babaeian et al., 2019; Serbin & Or, 2005). Compared with EMI that measures the apparent bulk electrical conductivity of the soil and is susceptible to temperature variations, GPR determines soil moisture by dielectric permittivity and is less sensitive to temperature fluctuations (Robinson, Campbell, et al., 2008). Besides, EMI usually produces results as a depth-weighted average (e.g., Robinson et al., 2012), whereas GPR can depict soil moisture patterns at different soil depths (e.g., Allroggen et al., 2015; Steelman et al., 2012). Compared with ERT, GPR has a faster rate of data collection, thereby allowing a broader spatial coverage and a shorter time interval between successive surveys (Robinson, Binley, et al., 2008). Given the good combination of detection depth, spatial coverage, and spatiotemporal resolution, GPR becomes a promising geophysical method of measuring soil moisture (Huisman et al., 2003; Klotzsche et al., 2018; Parsekian et al., 2015). The root-mean-square error (*RMSE*) between the RZSM estimated with GPR and the true values measured with conventional techniques can be as low as 0.010 $m^3 \cdot m^{-3}$ under controlled conditions (Grote et al., 2002; Stoffregen et al., 2002) and 0.018 $m^3 \cdot m^{-3}$ in natural settings (Liu, Cui, et al., 2019; Lunt et al., 2005).

To date, a series of GPR-based methods, including the reflected wave, ground wave, surface reflection, full waveform inversion, average envelope amplitude, and frequency shift methods, have been developed for various GPR systems (e.g., ground-coupled, air-coupled, and borehole systems) to map soil moisture (e.g., Jonard et al., 2017; Klotzsche et al., 2018; Liu, Chen, et al., 2019; Tosti & Slob, 2015; Vereecken et al., 2014). Borehole GPR requires the excavation of access tubes and has a limited survey area (Slob et al., 2010), while air-coupled GPR is most effective for measuring the soil moisture of the top few centimeters of the soil (Huisman et al., 2003; Qin et al., 2013). Therefore, ground-coupled GPR, which can be used to collect data to a depth of several meters and does not disturb soil conditions (Benedetto et al., 2017; Vereecken et al., 2014), is best-suited for the noninvasive measurement of RZSM. In particular, ground-coupled GPR with a fixed transmitter-receiver offset system (i.e., GPR-FO, also the most popular commercial GPR system) allows field measurements with broad coverage and a fast data collection speed (Huisman et al., 2003; Liu, Chen, et al., 2019; Zajícová & Chuman, 2019).

The reflected wave method developed for GPR-FO (hereinafter called the FO reflected wave method), which uses the velocity of the GPR reflected wave to estimate soil moisture (see details in section 2.1), has been considered promising in the noninvasive mapping of RZSM at field scales (Huisman et al., 2003; Lunt et al., 2005). However, previous studies were limited to applying the FO reflected wave method to measure the average RZSM under controlled conditions and at a single location (Liu, Cui, et al., 2019; Lunt et al., 2005; Stoffregen et al., 2002). Using this method to map the spatial variability of RZSM under real-world conditions at the field scale has been largely impeded by the lack of natural reflectors and the estimation of soil moisture at certain depths (see details in section 2.2).

The objective of this study is, therefore, to develop a new FO reflected wave method that can map the spatial distribution of RZSM in both 2D and 3D. To this end, we developed a method that combines the automatic identification of coarse root (diameter > 5 mm) reflections in GPR images with the spatial interpolation techniques to map RZSM. The proposed method was then tested in two plots (each of 900 m^2) in shrublands with sandy soil. To the best of our knowledge, this is the first study that applies GPR to map the spatial distribution of RZSM to the depths of approximately 1 m deep under real-world conditions at the field scale. This study enhances the application of near-surface geophysics for in situ measurement of soil moisture at intermediate scales, which complements the widely available point-based and large-scale remote sensing measurements of soil moisture, especially in the subsoil.

2. Principles of GPR-Based Soil Moisture Measurement and a New Possibility for Mapping RZSM

2.1. GPR-Based Soil Moisture Mapping and Its Limitations

In principle, GPR detects contrasts in the dielectric permittivity of subsurface media (Huisman et al., 2003). Because most geologic materials have dielectric permittivity in the range of 3 to 30, while the dielectric permittivity of water is 81 (Reynolds, 1997), even small changes in soil moisture, in space or time, will significantly alter radar reflection patterns (both wave velocity and reflection amplitude). The FO reflected wave method works by calculating the velocity of the reflected wave as it propagates through the soil and using this to estimate soil moisture (Stoffregen et al., 2002). In low-conductive, nonmagnetic, and nonsaline soils, the propagation velocity of a GPR reflected wave, v_{soil}, can be approximated as

$$v_{soil} \approx \frac{c}{\sqrt{\varepsilon_{soil}}}, \tag{1}$$

where ε_{soil} is the dielectric permittivity of the soil and c is the free space electromagnetic propagation velocity (i.e., 0.3 m·ns^{-1}; Huisman et al., 2003). Topp et al. (1980) developed an empirical relationship between volumetric soil moisture content (θ_{soil}) and dielectric permittivity:

$$\theta_{soil} = 4.3 \times 10^{-6} \times {\varepsilon_{soil}}^{3} - 5.5 \times 10^{-4} \times {\varepsilon_{soil}}^{2} + 2.92 \times 10^{-2} \times \varepsilon_{soil} - 5.3 \times 10^{-2}. \tag{2}$$

Once the wave velocity is obtained, soil moisture can be calculated using equations (1) and (2).

Two aspects of this approach have impeded its application in mapping RZSM (Liu, Chen, et al., 2019): (1) It relies on the existence of subsurface reflectors to generate the reflected wave (Stoffregen et al., 2002), so a certain number of reflectors must be identified across the targeted area to ensure reliable measurements of RZSM (Lunt et al., 2005); and (2) prior knowledge of the depths of subsurface reflectors is required, especially if a flat reflector is used, such as a soil layer or the capillary fringe (e.g., Wollschläger & Roth, 2005). The reflected wave velocity is calculated as the ratio between the depth of a given reflector and the travel time from the antenna to the reflector (Vereecken et al., 2014; Zajícová & Chuman, 2019). Therefore, the depths of the reflectors must be determined, either by excavating them after the measurements are made or by burying reflectors at known depths under controlled conditions (e.g., Lunt et al., 2005). Either way, the process is destructive to the soil environment, time consuming, and inconvenient for mapping RZSM in the field. Additionally, because the obtained velocity is the average value of the reflected wave traveling from the reflector to the ground surface, the common FO reflected wave method provides the average soil moisture from the surface to a given depth, that is, the profile soil moisture (Huisman et al., 2003; Steelman & Endres, 2012). Profile soil moisture is meaningful for studying many ecohydrological processes, such as plant available water and water budget in the terrestrial ecosystem, but provides limited information on the spatial variability of soil moisture at different depths. Therefore, to delineate the spatial variability of RZSM in 2D and 3D, much attention also should be paid to estimating the spatial distribution of interval soil moisture of a given soil layer.

2.2. A New Possibility to Enhance the FO Reflected Wave Method

Recently, GPR has been used for noninvasive detection and quantification of plant coarse roots under various field conditions (Guo et al., 2013a). Some studies have successfully applied GPR for automatic positioning of roots (Li et al., 2016), mapping the extent of the root zone (Hruška et al., 1999), identifying root branching patterns (Guo et al., 2015; Zhu et al., 2014), reconstructing root system architectures and profiles (Cui et al., 2020; Wu et al., 2014), and measuring root biomass (Butnor et al., 2003; Guo et al., 2013b; Molon et al., 2017). When measuring coarse roots, a GPR antenna transmits electromagnetic pulses into the subsurface and receives echoes that are backscattered from root reflectors (Figure 1a). Because the GPR energy propagates as a wide beam through the subsurface, a coarse root can be detected even if the antenna is not directly above it. The travel time of reflected wave from the antenna to the root reaches its minimum when the GPR antenna is right above the root (Guo et al., 2013a). This phenomenon causes a coarse root to form a hyperbolic reflection in GPR images (Figures 1a and 1c). The geometric relationship of such a hyperbolic reflection can be described as (Huisman et al., 2003)

$$\frac{{t_w}^2}{\left(\frac{2\times h_{root}}{v_{soil}}\right)^2} - \frac{x^2}{{h_{root}}^2} = 1, \tag{3}$$

where v_{soil} is the velocity of the reflected wave, x is the horizontal distance of the GPR antenna relative to the coarse root, t_w is the two-way travel time from GPR antenna to the coarse root, and h_{root} is the depth of a coarse root. Therefore, the moisture of the intervening soil, which determines its dielectric permittivity

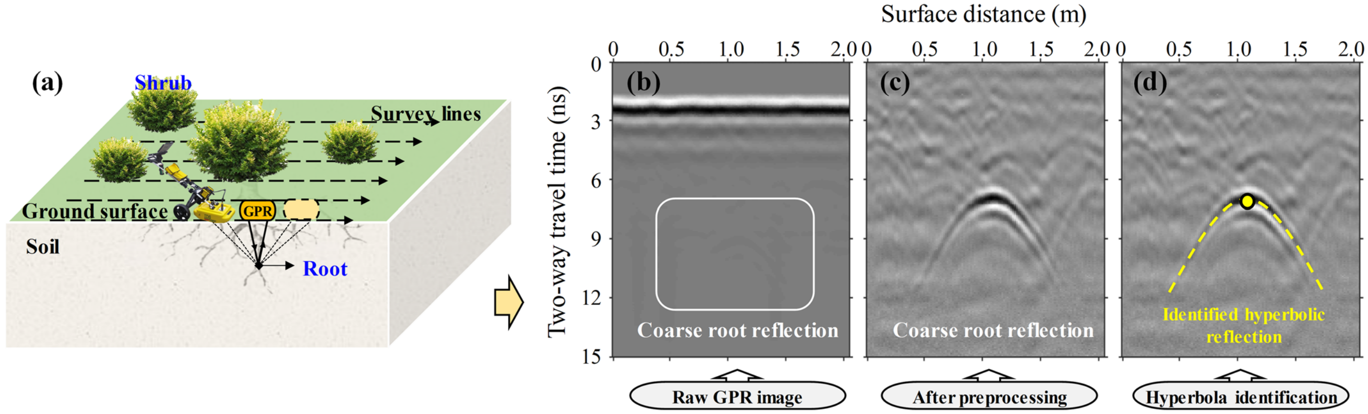

Figure 1. (a) A scheme of the survey lines and the process of GPR-FO detection of coarse roots. (b) A raw GPR image collected by a 900-MHz antenna, including a blurry hyperbolic reflection formed by a coarse root. (c) After preprocessing, a clear image of the coarse root reflection was produced. (d) An illustration of the automatic hyperbola identification algorithm implemented on the GPR image. Both the root location (indicated by the yellow dot) and the velocity of the reflected wave propagating through the soil were obtained after the coarse root reflection was automatically identified (indicated by the yellow dash hyperbolic curve). The shape of a hyperbola, that is, its opening angle, is closely related to wave velocity, which can be determined by solving equation 3.

and the velocity of the reflected wave (equations 1 and 2), is the key control of the shape of a coarse root reflection in GPR images. The higher the soil moisture, the tighter the angle between the two limbs of a hyperbolic reflection produced by a coarse root (Li et al., 2016). Based on this principle, Liu, Cui, et al. (2019) recently verified that plant coarse roots could be employed as natural reflectors for use in the FO reflected wave method to measure RZSM.

An algorithm for the noninvasive determination of the velocity of a reflected wave from a single coarse root reflection in GPR images, or "automatic hyperbola identification algorithm," has already been established (Li et al., 2016; Liu, Cui, et al., 2019). This algorithm obtains the reflected wave velocity in three steps:

1. Raw GPR images are preprocessed to highlight coarse root reflections, such as the removal of the direct current component by detrending, the removal of low-frequency and high-frequency noise by dewow filtering and low-pass filtering, respectively, suppressing the banding noise due to antenna reverberation by background removal, and compensating GPR energy attenuation by amplitude gain (Guo et al., 2013a; Liu, Cui, et al., 2019). Examples of coarse root reflections before and after preprocessing are compared in Figures 1b and 1c.
2. Regions of interest (ROIs) of a hyperbola in GPR images are generated by the Sobel filter (Dim & Takamura, 2013), an image edge extraction operator that aims to facilitate the automatic identification of hyperbolas.
3. Randomized Hough Transform method is applied to seek hyperbolic patterns within each ROI. In each iteration, three points from a ROI edge will be randomly selected to solve the unknown parameters (i.e., v_{soil}, h_{root}, and x) of equation (3). Then, the occurrence frequency of the solved set of parameters is recorded. This process repeats until the number of the iteration reaches a pre-set threshold. The parameter set with the highest occurrence frequency is considered the parameters for the identified hyperbola curve. By doing this, the velocity of the reflected wave and root depth are determined. More detailed descriptions of hyperbola identification and velocity estimation can be found in Li et al. (2016), Liu, Cui, et al. (2019), and Xu and Oja (1993).

With this approach, prior knowledge of root depth is no longer required, and the reflected wave velocity is calculated without disturbing the soil environment. By considering coarse roots as natural reflectors that are widely distributed throughout the root zone, the automatic hyperbola identification algorithm is promising in enhancing the FO reflected wave method to map RZSM at the field scales.

3. A Novel Method that Uses GPR to Characterize RZSM

In this study, we propose a new FO reflected wave method to map RZSM by automatically identifying coarse root reflections in GPR images (Li et al., 2016; Liu, Cui, et al., 2019) and the spatial interpolation of soil

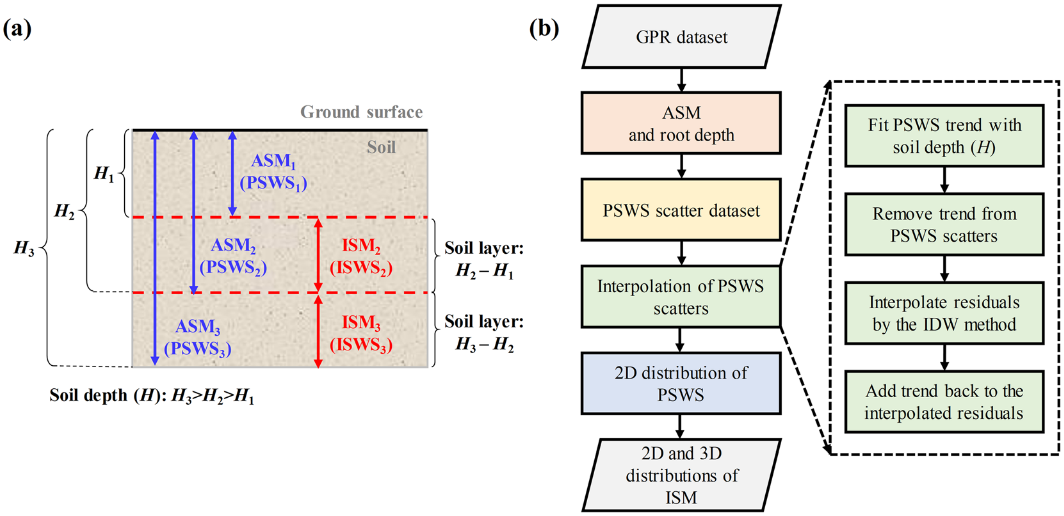

Figure 2. (a) Definitions of ASM, ISM, PSWS, and ISWS. The average soil moisture (or soil water storage) from the ground surface to the three soil depths of H_1, H_2, and H_3 are defined as ASM$_1$ (or PSWS$_1$), ASM$_2$ (or PSWS$_2$), and ASM$_3$ (or PSWS$_3$), respectively. The average soil moisture (or soil water storage) for the soil layers of $H_2 - H_1$ and $H_3 - H_2$ are defined as ISM$_2$ (or ISWS$_2$) and ISM$_3$ (or ISWS$_3$), respectively. (b) A flowchart depicting the process of estimating 2D and 3D distributions of ISM from a GPR data set of coarse root reflections collected at various depths and horizontal locations over a root zone.

moisture derived from each identified root reflection. The newly established protocol aims to enhance the method presented in Liu, Cui, et al. (2019) in three aspects: (1) extending the application scope from controlled conditions at a single location to real-world conditions at field scales, (2) extending the results from average profile soil moisture at a single location to 2D horizontal distributions of soil moisture at different soil depths, and (3) 3D visualization of the spatial distribution of soil moisture in the root zone.

Before we can articulate this method, we need to define four soil moisture-related parameters (Figure 2a): (1) average soil moisture (ASM) from the ground surface to a given depth; (2) average interval soil moisture (ISM) of a given soil layer; (3) soil water storage from the surface to a given depth, or profile soil water storage (PSWS); and (4) soil water storage of a given soil layer, or interval soil water storage (ISWS). Here, soil moisture ($m^3 \cdot m^{-3}$) estimated by the proposed method refers to the volumetric soil water content, which is the volume of liquid water per volume of soil, and soil water storage (mm) estimated by the proposed method refers to the amount of water stored in the soil, and it can be calculated as the sum of volumetric soil water content within a certain depth range.

The proposed method consists of four primary steps (Figure 2b): (1) retrieving the ASM and root depth from coarse root reflections in GPR images; (2) generating a data set of PSWS scatters; (3) interpolating these PSWS scatters into 2D distributions of PSWS to different soil depths; and (4) 2D and 3D visualization of ISM. Each step is detailed below.

3.1. Retrieving ASM and Root Depth

The automatic hyperbola identification algorithm (Li et al., 2016; Liu, Cui, et al., 2019; also see section 2.2) is performed on GPR images to recognize coarse root reflections and obtain the average velocity of the reflected wave between the surface and the root reflector as well as the root depth for each identified coarse root reflection (Figures 1 and 3). The average velocity is then used to calculate the average soil dielectric permittivity with equation (1), which is further converted into the ASM above the coarse root using the empirical (e.g., Topp's equation) or an in situ calibrated relationship between soil moisture and dielectric permittivity.

3.2. Generating a Data Set of PSWS Scatters

After ASM and root depth are obtained for an identified coarse root, the corresponding PSWS (mm) to the root depth, h_{root} (m), is calculated as

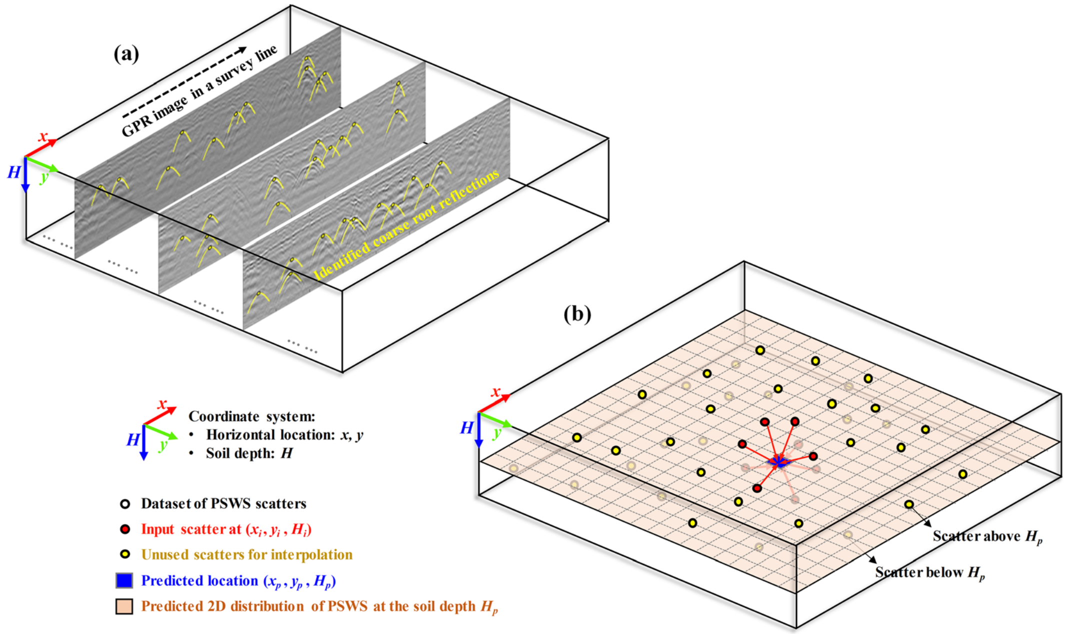

Figure 3. (a) An example of the automatic hyperbola identification algorithm applied to GPR images collected on three parallel survey lines. Numerous coarse root reflections were identified, and the corresponding root depth and wave velocity were obtained for each coarse root reflection. These velocities and root depths were used to compute PSWSs by equations (1), (2), and (4), yielding a data set of PSWS scatters. (b) Performing the IDW interpolation on the data set of PSWS scatters to generate a 2D distribution of PSWS at the soil depth of H_p.

$$\mathrm{PSWS} = \mathrm{ASM} \times h_{root} \times 1,\ 000, \tag{4}$$

where 1,000 is the conversion coefficient from m to mm. For n identified coarse root reflections (Figure 3a), n discrete PSWSs are generated at various locations throughout the root zone, leading to a data set of PSWS scatters in the (x, y, H) space, $PSWS(x, y, H)$, where x and y indicate the horizontal location coordinates and H indicate the soil depth (Figure 3b). The ith scatter of PSWS was denoted as PSWS (x_i, y_i, H_i), referring to the PSWS from the surface to soil depth of H_i and at the horizontal location of (x_i, y_i).

3.3. Mapping 2D Distributions of PSWS

We propose to use the inverse distance weighted (IDW) interpolation with the trend model to reconstruct the 2D distributions of PSWS at a predicted soil depth, H_p. The IDW interpolation method sets the attribute value at a given predicted location as the weighted average of the known values, with the weights inversely related to the distances between the predicted location and the sampled locations. Moreover, the IDW method assumes that the influence of sampled locations on the predicted location is isotropic (Lu & Wong, 2008). Given the nature of PSWS that always increases with soil depth, we perform detrending on it before spatial interpolation. The purpose of detrending is to remove the directional bias caused by the trend of the predicted variable (PSWS in our case). Previous studies confirmed an improved performance of spatial interpolation with the trend being considered (e.g., Jost et al., 2005; Snepvangers et al., 2003; Yang et al., 2015). In this study, the spatial variable of $PSWS(x, y, H)$ is assumed to have the decomposition of

$$PSWS(x,\ y,\ H) = T(H) + R(x,\ y,\ H), \tag{5}$$

where the spatial variable of $PSWS(x, y, H)$ has two components, including a mean component representing the general trend of the accumulation of soil water with soil depth, denoted as $T(H)$ and a residual component of soil water storage that deviates from the trend to account for local variations, denoted as $R(x, y, H)$. Then, the IDW interpolation will be performed on the residuals, and the trend will be added back to the IDW prediction to produce the final interpolation maps. Nevertheless, the proposed method does not reject the use of other methods (e.g., the ordinary Kriging) for spatial interpolation. A comparison between different interpolation methods is beyond the scope of the current study.

The spatial interpolation of PSWS scatters takes four steps:

Step 1: Fitting the trend model of PSWS against soil depth to obtain $T(H)$. We use a linear model to define the trend,

$$T(H) = a \times H + b, \tag{6}$$

where a and b are model parameters determined by fitting the linear model with all obtained PSWS scatters.

Step 2: Detrending. The trend component of PSWS at the soil depth of H_i, $T(H_i)$, is removed from each of the PSWS scatters, $PSWS(x_i, y_i, H_i)$, to obtain the local residual of soil water storage, $R(x_i, y_i, H_i)$

$$R(x_i, y_i, H_i) = PSWS(x_i, y_i, H_i) - T(H_i),\ i = 1,\ 2,\ \cdots,\ n, \tag{7}$$

where n is the number of the scatters obtained.

Step 3: Spatial interpolation. The scatters of $R(x_i, y_i, H_i)$ are spatially interpolated into 2D distributions of the residual of soil water storage to different predicted locations (x_p, y_p, H_p) by adopting the IDW method (Li et al., 2014),

$$R\left(x_p, y_p, H_p\right) = \sum_{i=1}^{m} \left(w_i \times R(x_i, y_i, H_i)\right), \tag{8}$$

$$w_i = \frac{\frac{1}{d_i}}{\sum_{n=1}^{m} \frac{1}{d_n}}, \tag{9}$$

where $R(x_p, y_p, H_p)$ indicates the residual at the predicted locations (x_p, y_p, H_p); $R(x_i, y_i, H_i)$ is the residual of ith input scatter at the sampled locations (x_i, y_i, H_i); w_i is the weight for the ith input scatter, which is determined by the Euclidean distance, d_i, between the predicted location (x_p, y_p, H_p) and the sampled location (x_i, y_i, H_i); and m is the total number of input scatters with the closest distance to the predicted location (x_p, y_p, H_p), that is, $m < n$, which are used to predict $R(x_p, y_p, H_p)$, as shown in Figure 3b.

Step 4: Retrending. We add $T(H_p)$ back to the interpolated residuals of soil water storage at each predicted location as

$$PSWS\left(x_p, y_p, H_p\right) = T\left(H_p\right) + R\left(x_p, y_p, H_p\right), \tag{10}$$

where $PSWS$ (x_p, y_p, H_p) is the profile soil water storage corresponding to the predicted location (x_p, y_p, H_p). After the values of PSWS for all pixels at the prediction depth of H_p are interpolated, the 2D distribution of PSWS to H_p, $P(H_p)$, is reconstructed (Figure 3b). By changing the value of H_p, the 2D distributions of PSWS to different soil depths are calculated.

3.4. Reconstructing 2D and 3D Distributions of ISM

After the 2D distributions of PSWS to different soil depths, such as H_1 and H_2, are obtained, we are able to calculate of the difference in profile soil water storage to those depths, for example, $P(H_2) - P(H_1)$. This difference represents the soil water storage of the soil layer from H_1 to H_2 (Figure 4). By dividing this soil water storage by the thickness of this soil layer, $H_2 - H_1$, we generate the 2D distribution of the average soil moisture for this soil layer, for example, $ISM(H_2 - H_1)$, by

$$ISM(H_2 - H_1) = \frac{(P(H_2) - P(H_1))}{1,\ 000 \times (H_2 - H_1)}, \tag{11}$$

or

$$ISM(H_3 - H_2) = \frac{(P(H_3) - P(H_2))}{1,\ 000 \times (H_3 - H_2)}, \tag{12}$$

where $P(H_1)$, $P(H_2)$, and $P(H_3)$ are the 2D distributions of PSWS at the soil depths of H_1, H_2, and H_3, respectively (Figure 4); $ISM(H_2 - H_1)$ and $ISM(H_3 - H_2)$ are the 2D distributions of ISM for the soil

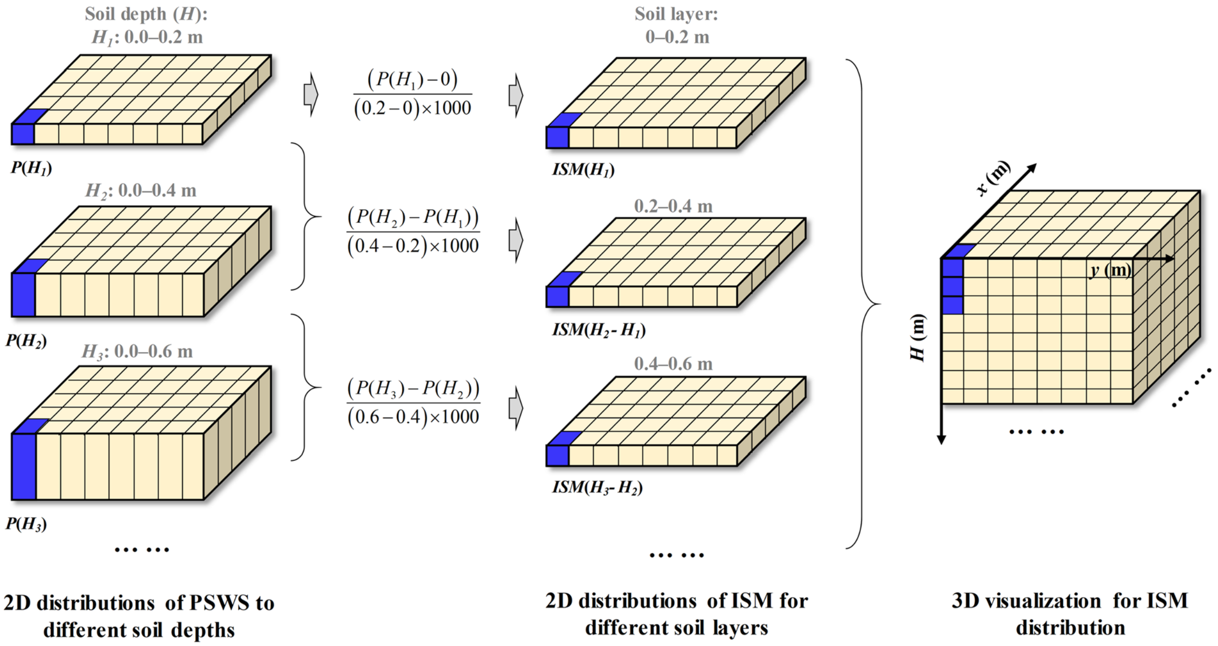

Figure 4. An illustration of constructing 2D and 3D distributions of ISM based on the 2D distribution of PSWS to different soil depths. The 2D distribution of PSWS to multiple soil depths (e.g., 0.0–0.2, 0.0–0.4, and 0.0–0.6 m) were first calculated as 2D distributions of ISM for the corresponding soil layers (e.g., 0.0–0.2, 0.2–0.4, and 0.4–0.6 m) by equations (11) and (12). Then, all 2D distributions of ISM were combined into a 3D volume of ISM for the 3D visualization of RZSM.

layers of $H_2 - H_1$ and $H_3 - H_2$, respectively (Figure 4); 1,000 is the conversion coefficient from m to mm. In this way, every pixel on a 2D distribution of ISM is computed from the corresponding pixels on the 2D distributions of PSWS at two soil depths by equations (11) and (12). Finally, we combine the 2D distributions of ISM for a series of soil layers into a 3D volume of ISM for a 3D visualization (Figure 4).

4. Field Validation

4.1. Site Description

The study site (43°55′01″N, 116°12′17″E, 1,082 m a.s.l.) is located in the Xilinguol of Inner Mongolia in northern China (Figure 5). This semiarid region has a temperate continental climate (Cao et al., 2018). Most of the 300 mm of mean annual precipitation falls during the growing season, from May through September (Zhao et al., 2011). The annual potential evapotranspiration is about 1,750 mm, and the mean annual air temperature is about 2.6°C (Chi et al., 2018; Yiruhan et al., 2014).

Caragana microphylla Lam is one of the dominant shrub species in this region (Cao et al., 2019). This species has a well-developed lateral root system that can spread 3.0 m away from the stem, with a rooting depth ranging from 0.2 to 1.5 m and the greatest root density at the depth of 0.4 to 0.6 m (Cui et al., 2020; Wang et al., 2017; Wu et al., 2014). Such a root system provides a large number of natural reflectors for applying the proposed method to map RZSM. Intershrub spaces are often occupied by perennial grasses, including *Stipa krylovii* Roshev., *Leymus chinensis* (Trin.) Tzvel., *Cleistogenes squarrosa* (Trin. ex Ledeb.) Keng, and *Artemisia frigida* Willd (Figure 6a). The roots of these grass species are dominated by fine roots (diameter < 5 mm), which are mainly distributed in the near-surface soil (<10 cm).

Previous in situ soil sampling indicated that the local soil texture types were sand and sandy loam. The average particle-size distribution of the soil was 62.20 ± 6.21% sand, 35.66 ± 6.04% silt, and 2.14 ± 0.99% clay. The soil bulk density was 1.63 ± 0.15 $\mathrm{g \cdot cm^{-3}}$. The local soil was relatively uniform and dry (with soil moisture usually <0.15 $\mathrm{m^3 \cdot m^{-3}}$). Soil organic content and clay content were low. These conditions favor the performance of GPR-based coarse root detection and quantification (Guo, Lin, et al., 2013b), which has been confirmed in previous studies in this area (e.g., Cui et al., 2013, 2020; Guo et al., 2015; Li et al., 2016; Wu et al., 2014).

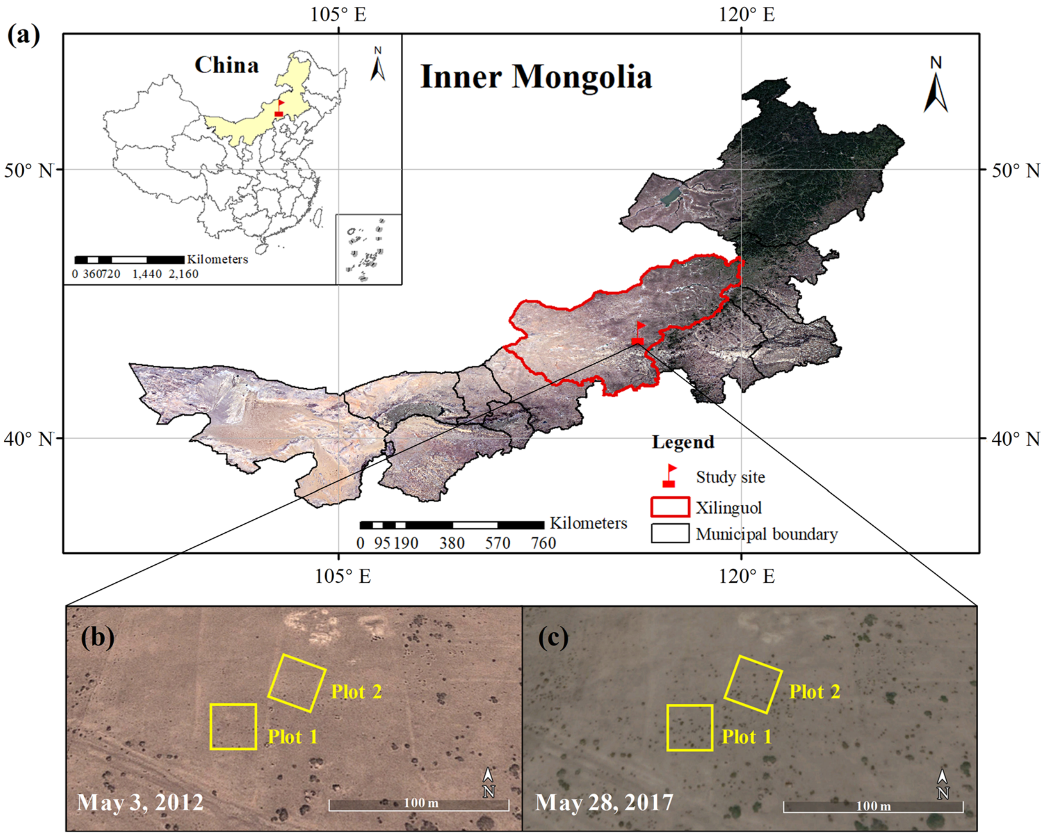

Figure 5. (a) The study site is located in Xilinguol, Inner Mongolia, northern China. This area is experiencing shrub encroachment, with *Caragana microphylla* Lam as the dominant shrub species. The well-developed lateral roots of *Caragana m.* provide natural reflectors for GPR measurements. (b, c) Satellite images (from Google Earth) collected on 3 May 2012 and 28 May 2017, respectively, demonstrate the increase in shrub coverage over the past five years. Two plots, namely, Plot 1 and Plot 2 (indicated by the yellow squares), were selected for GPR scanning.

4.2. Data Collection

Two 30 m by 30 m plots (spaced 30 m apart) were selected (Figure 5b). Plot 1 was located on a relatively flat area, while Plot 2 was located on a gently sloping area with a slope inclination of ~10°, dipping from northeast to southwest. Both plots had the same vegetation types, mainly including *Caragana microphylla* Lam and perennial grasses. Due to the different stages of the growing season, the vegetation cover presented different growth statuses between two plots (Figure 6a). Biometric parameter measurements, GPR surveys, and ground truthing data collection were conducted on 12 July 2017 for Plot 1 and 17 August 2018 for Plot 2 (Figure 6). The experimental procedures were identical for both plots.

4.2.1. Biometric Parameter Measurements

The number, location, and canopy area of each shrub in the study plot were recorded (Figure S1 in the supporting information). There were 58 shrubs with an average canopy area of 1.45 m^2 per shrub in Plot 1 and 46 shrubs with an average canopy area of 1.80 m^2 per shrub in Plot 2. The distribution patterns of shrubs were used to compare with the spatial variability of RZSM derived by GPR surveys.

4.2.2. GPR Surveys

After biometric parameter measurements were taken, the ground surface was cleaned of surface debris, and the above-ground parts of the shrubs were removed to allow GPR scanning of the entire plot and adequate comparisons with results from soil augering. The GPR images were collected in each plot along 121 parallel survey lines (each 30 m long, spaced 0.25 m apart; Figure 6b). The dense spacing between survey lines ensured complete coverage over the entire plot, which maximized the detection frequency of coarse roots by GPR. We used a ground-coupled GPR system (RIS MF HI-MOD, Ingegneria Dei Sistemi Inc., Pisa, Italy) with a fixed constant offset of 0.15 m between the transmitter and the receiver. The central frequency of the GPR system was 900 MHz, which provided the best combination of detection resolution (i.e., image

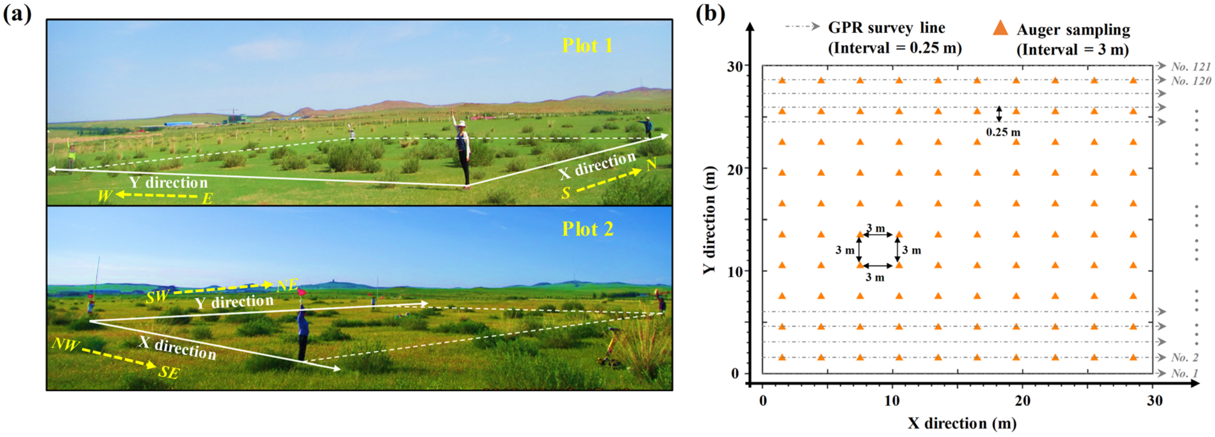

Figure 6. (a) Field photographs of the two shrub plots on the experiment dates, 12 July 2017 (in the middle of the growing season) for Plot 1 and 17 August 2018 (near the end of the growing season) for Plot 2. (b) A diagram of the layout of GPR survey lines (indicated by the dashed lines) and the auger sampling grid (indicated by the triangles) for both plots. The interval between neighboring GPR survey lines was 0.25 m, and the interval between adjacent auger holes was 3 m.

quality), depth penetration, and operational convenience according to previous GPR studies under similar site conditions (e.g., Guo et al., 2013c; Guo, Lin, et al., 2013b; Wu et al., 2014). The GPR data set was acquired with a time window of 30 ns and a sampling interval of 0.0586 ns per trace, which yielded 512 samples per trace. A survey wheel triggered GPR data collection every 1.6 cm along the survey line. It required approximately 2.5 hr for GPR scanning all 121 survey lines. It is worthwhile to mention that the removal of the vegetation cover, which was done in this study to facilitate the validation of the method, is not a requirement of the proposed method. Especially for long-term, repeated GPR surveys, it is recommended to keep the vegetation cover to explore the dynamics of vegetation-soil moisture feedback over time (e.g., Cui et al., 2020).

4.2.3. Ground Truth Data

Soil cores were augured on a 3-m grid across the entire plot to obtain actual measurements of RZSM to compare with our GPR survey estimates, yielding a total of 100 evenly distributed augering locations in each plot (Figure 6b). At each augering location, gravimetric soil moisture content was measured at depth intervals of 0.0–0.2, 0.2–0.4, 0.4–0.6, and 0.6–0.8 m in Plot 1, and 0.0–0.1, 0.1–0.3, 0.3–0.5, and 0.5–0.7 m in Plot 2 by oven drying the soil cores until a constant weight was reached. Additionally, soil cores were collected to measure the soil bulk density at each soil layer interval, which were used to covert the gravimetric soil moisture content into volumetric soil moisture content to calculate PSWS (mm)

$$PSWS_{auger} = \sum_{k=1}^{N} \left(ISM_k \times T_k \times 1,\ 000 \right), \tag{13}$$

where k is the kth sampled soil layer, N is the total number of sampled soil layers, $PSWS_{auger}$ (mm) is the profile soil water storage obtained from augering data, ISM_k ($\mathrm{m}^3\ \mathrm{m}^{-3}$) is the measured volumetric soil moisture content of the kth soil layer, and T_k (m) is the thickness of the kth soil layer; 1,000 is the conversion coefficient from m to mm. Point-based soil moisture and soil water storage measurements obtained by augering were interpolated into 2D distributions using the IDW interpolation as well, so that they were comparable with the GPR-derived maps.

4.3. Application of the Proposed Method

First, the raw GPR data set collected in the field was preprocessed by several standard procedures: Zero-time correction adjusted the radar signal to start from the ground surface, background removal eliminated noise, and amplitude compensation corrected for GPR energy attenuation with penetrating depth (Guo et al., 2013a). After the preprocessing, the depth and horizontal locations of each identified coarse root in the GPR images, as well as the average velocity of the reflected wave between the surface and root depth, were determined by the automatic hyperbola identification algorithm. Then, ASM was computed at the location of each root. Here, we employed Topp's equation (equation 2) to rapidly determine ASM in

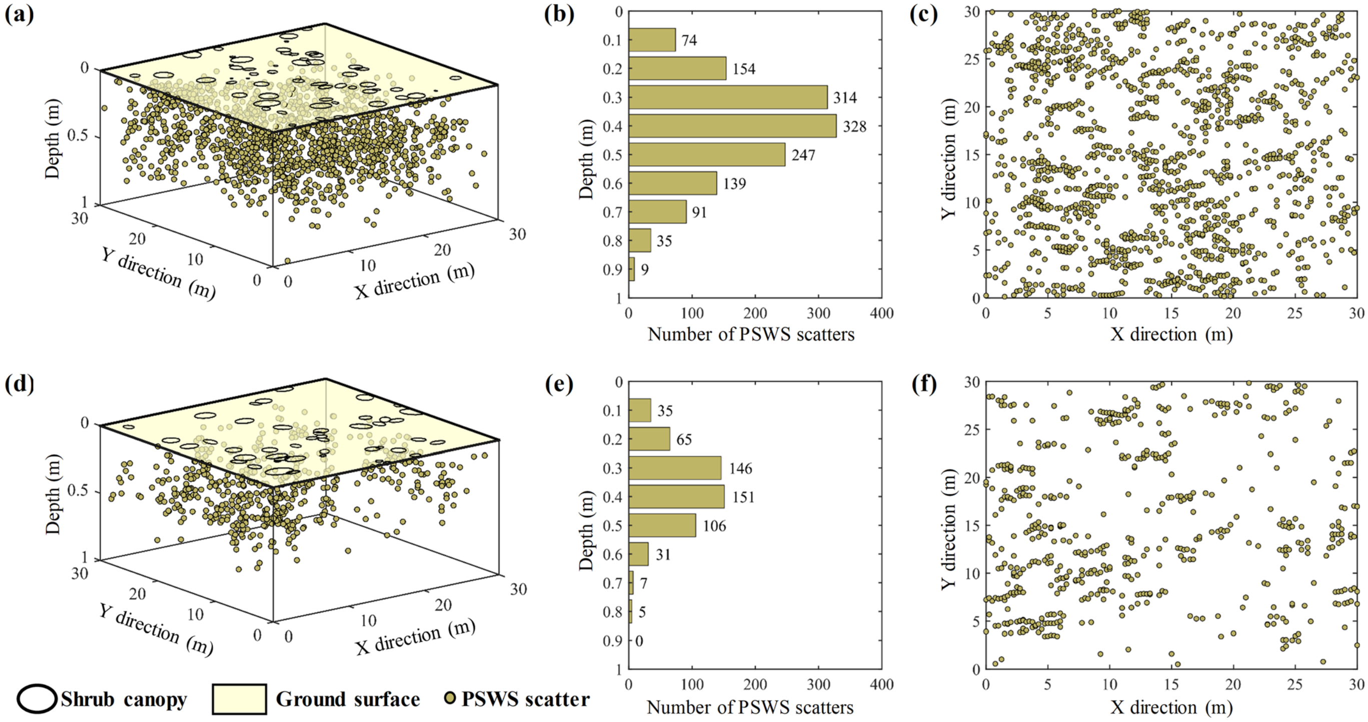

Figure 7. Distributions of PSWS scatters in both plots are displayed in a 3D view (a,d), as histograms with the depth (b,e), and in a top-down view (c,f). (a–c) are for Plot 1, and (d–f) for Plot 2.

consideration of its successful application at the study site (Liu, Cui, et al., 2019). See details of these processes in Figure S2.

Second, scatters of PSWS for two plots were generated from the obtained ASM values using equation (4). The total number of PSWS scatters was 1,391 in Plot 1 and 546 in Plot 2. The relative frequency of PSWS scatters with soil depth demonstrates a unimodal distribution. Most PSWS scatters were distributed at depths from 0.2 to 0.7 m in both plots (Figures 7b and 7e). Moreover, PSWS scatters were evenly distributed across the horizontal projection plane (Figures 7c and 7f), ensuring reliable spatial interpolation from discrete PSWS scatters to the 2D distribution of PSWS.

Third, the scatters of PSWS in both plots were interpolated into the 2D horizontal distributions of PSWS to various soil depths. To determine the PSWS trend model parameters of a and b, all PSWS scatters in each plot were grouped at the depth intervals of 0.1 m, which matched the soil layers for which ISM was subsequently estimated and provided enough scatters to calculated their average for a depth interval. Then, the average values of PSWS scatters within every depth interval were computed and fitted by the trend model (equation 6). The model parameters, a and b, were respectively determined to be 68.01 and −4.90 for Plot 1 and 77.66 and −4.78 for Plot 2 (Figure S3). For the spatial interpolation of $R(x_p, y_p, H_p)$, the horizontal location coordinates, x_p and y_p, were set to the range of 0 to 30 m for both plots, and the predicted soil depth, H_p, was set to the range of 0.1 to 0.9 m for Plot 1 and 0.1 to 0.8 for Plot 2, respectively, to account for the vertical distribution range of PSWS scatters (Figure 7). Because the vertical resolution of the selected 900-MHz GPR system at the study site was about 0.08 m (Liu, Cui, et al., 2019), the depth increment of H_p used to reconstruct the 2D distribution of PSWS to a certain depth was set to 0.1 m, given that the vertical resolution declined with soil depth due to the dispersion of antenna center frequency (Rial et al., 2009). In this way, the 2D horizontal distributions of PSWS were reconstructed at nine depths in Plot 1 and eight depths in Plot 2. The horizontal resolution of the 2D distributions of PSWS, that is, the size of a pixel for spatial interpolation (Figure 3b), was set to 0.1 × 0.1 m in both plots. It should be noted that the selection of the depth interval to group PSWS scatters to determine the trend model (equation 6) and for spatial interpolation is site-specific, which is influenced by the vertical resolution of the selected GPR at a given site and the number of the detected roots.

Finally, the 2D distributions of ISM for soil layers of 0–0.2, 0.2–0.4, 0.4–0.6, and 0.6–0.8 m deep in Plot 1 and 0.1–0.3, 0.3–0.5, and 0.5–0.7 m deep in Plot 2 were computed using equations (11) and (12) to compare with augering results. For a high-resolution visualization of the 3D distribution of ISM, the 2D distributions of ISM in consecutive soil layers, with an interval of 0.1 m, were stacked to generate a 3D data cube using MATLAB (The MathWorks, Inc., Natick, MA, USA).

4.4. Comparisons Between Augering Measurements and GPR-Derived Results

Different statistic metrics were calculated to compare 2D distributions of GPR-derived PSWS and ISM to results from augering measurement. The Pearson correlation coefficient (*r*) and *RMSE* were used to evaluate the degree of agreement and prediction precision between GPR-derived and augering results, respectively. Given the difference in the magnitude of PSWS and ISM value with depth, the relative *RMSE* (*RRMSE*) was calculated to enable an intercomparison of GPR-derived results among different soil depths. In addition, standard deviation (*STD*) was employed to characterize the spatial variability of RZSM at a certain soil depth.

$$r = \frac{\sum_{j=1}^{N}\left[\left(D_j{}^{GPR} - D^{-GPR}\right) \times \left(D_j{}^{Auger} - D^{-Auger}\right)\right]}{\sqrt{\sum_{j=1}^{N}\left(D_j{}^{GPR} - D^{-GPR}\right)^2} \times \sqrt{\sum_{j=1}^{N}\left(D_j{}^{Auger} - D^{-Auger}\right)^2}}, \tag{14}$$

$$RMSE = \sqrt{\frac{1}{N} \times \sum_{j=1}^{N}\left(D_j{}^{GPR} - D_j{}^{Auger}\right)^2}, \tag{15}$$

$$RRMSE = \frac{RMSE}{\overline{D}^{GPR}} \times 100\%, \tag{16}$$

$$STD = \sqrt{\frac{1}{N-1} \times \sum_{j-1}^{N}\left(D_j{}^{GPR} - \overline{D}^{GPR}\right)^2}, \tag{17}$$

where $D_j{}^{GPR}$ and $D_j{}^{Auger}$ are the value of each pixel in the 2D distribution of PSWS (or ISM) derived by GPR and augering measurements at the same soil depth, respectively; *N* is the number of pixels in the 2D distribution of PSWS or ISM; and $\overline{D}^{GPR}$ and $\overline{D}^{Auger}$ represent the mean value of *N* pixels.

5. Results

5.1. Two-Dimensional Distributions of PSWS

The 2D distributions of PSWS derived by the proposed GPR method were compared with the actual measurements by augering in Figure 8 for Plot 1 and Figure 9 for Plot 2. Overall, the two methods resulted in comparable spatial patterns of PSWS in both plots for all investigated thicknesses of the soil profile, including 0.0–0.2, 0.0–0.4, 0.0–0.6, and 0.0–0.8 m in Plot 1 (Figure 8) and 0.0–0.3, 0.0–0.5, and 0.0–0.7 m in Plot 2 (Figure 9), respectively. The correlation coefficients between the PSWS obtained by the two methods ranged from 0.402 to 0.826 at different depths. For the topsoil (0.2 m depth in Plot 1 and 0.3 m depth in Plot 2), GPR-derived PSWS underestimated the true values (Figures 8a–8c and 9a–9c). The limited number of PSWS scatters upon which the spatial interpolation was performed (Figure 7) likely led to the discrepancy between estimation and actual measurement in the topsoil. Nevertheless, the general spatial distribution of GPR-derived PSWS matched the augering data in both plots. For example, both methods revealed a relatively dry area in the center of Plot 1 (Figures 8a and 8b) and a relatively wet area in the lower right corner of Plot 2 (Figures 9a and 9b).

As the thickness of the investigated soil profile increased, the GPR-derived PSWS and the augering measurements were distributed evenly on both sides of the 1:1 line (Figures 8c, 8f, 8i, 8l and 9c, 9f, 9i), indicating a good match between the estimation and observation in both plots. The correlation coefficients between GPR-derived PSWS and the augering data were all greater than 0.772 for thick soil profiles (i.e., >0.4 m in Plot 1 and >0.5 m in Plot 2), with *RRMSE* values lower than 7.4%. The spatial variation in the GPR-derived PSWS closely resembled that of the augering data (Figures 8d–8e, 8g–8h, 8j–8k and 9d–9e,

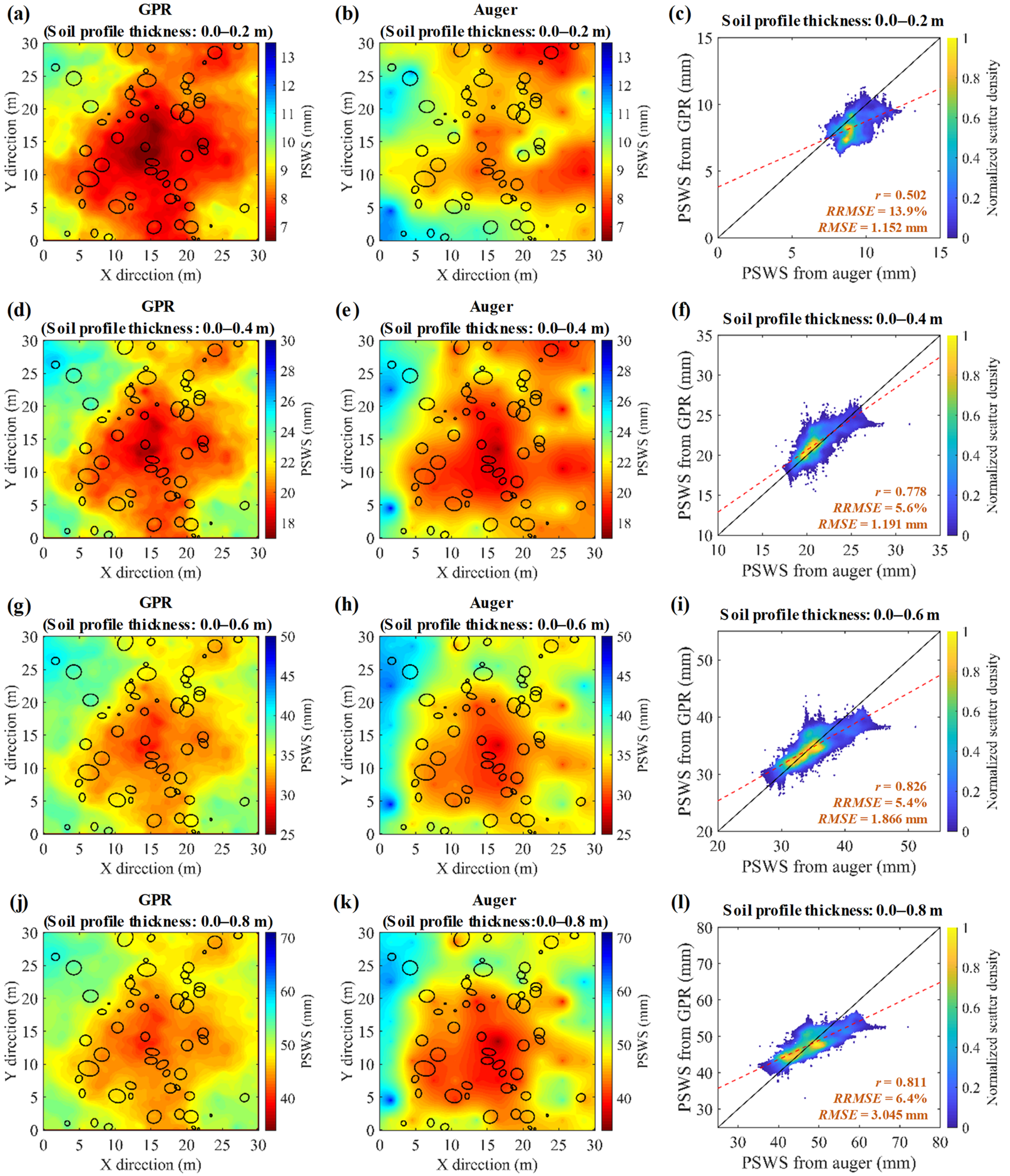

Figure 8. Comparisons of PSWS distributions estimated from the GPR method (a,d,g,j) and auger sampling (b,e,h,k) to different soil depths in Plot 1. The distribution and size of the above-ground shrub canopies are indicated by the open ovals. (c,f,i,l) Density scatter plots of PSWSs estimated from GPR and augers to soil depths of 0.2, 0.4, 0.6, and 0.8 m, respectively. The red dashed line indicates the linear regression model between estimates from GPR and measurements from augering. The black line is the 1:1 relationship. The color bar indicates the density of scatters.

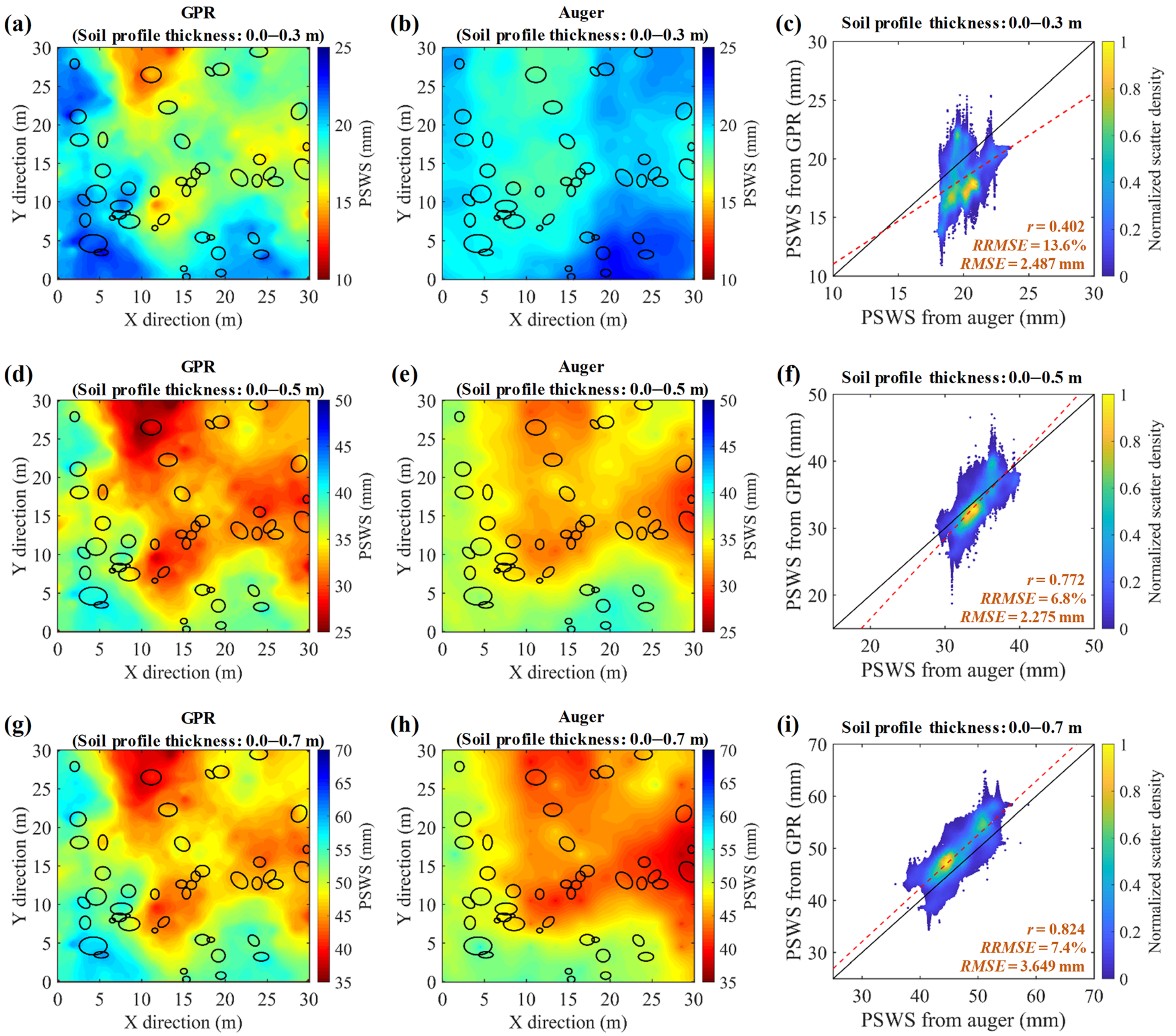

Figure 9. Comparisons of PSWS distributions estimated from the GPR method (a,d,g) and auger sampling (b,e,h) to different soil depths in Plot 2. The distribution and size of the above-ground shrub canopies are indicated by the open ovals. (c,f,i) Density scatter plots of PSWSs estimated from GPR and augers at soil depths of 0.3, 0.5, and 0.7 m, respectively. The red dashed line indicates the linear regression model between estimates from GPR and measurements from augering. The black line is the 1:1 relationship. The color bar indicates the density of scatters.

9g–9h). All localized wet spots and dry spots that were identified by augering were captured in the 2D distributions of GPR-derived PSWS, such as the dry area in the center of Plot 1 (Figures 8d–8e, 8g–8h, and 8j–8k), three dry spots spreading from the top to the center and to the right of Plot 2, and a wet area in the lower-left corner in Plot 2 (Figures 9d–9e and 9g–9h).

The accuracy of GPR-derived PSWS peaked at soil profile thicknesses of 0.4 to 0.6 m for Plot 1 and 0.5 m for Plot 2. With further increases in the thickness of the investigated soil profile, the accuracy of PSWS estimation declined, as indicated by the larger *RRMSE*. The relationship between the accuracy of PSWS estimation and soil depth was consistent with the vertical distribution of the PSWS scatters (Figure 7), which also showed a unimodal distribution against soil depth (Figure S4). In addition, the accuracy of the PSWS estimates was higher in Plot 1 than in Plot 2, as shown by lower *RRMSE* values and higher correlation coefficients. This could be explained by the higher distribution density of PSWS scatters in Plot 1 (Figure 7).

5.2. Two-Dimensional Distributions of ISM

The 2D distributions of ISM derived by the proposed GPR method were compared with the augering results for various soil layers in Figures 10 and 11. To facilitate the comparison between the two plots and different soil depths, the thicknesses of all soil layers used to calculate ISM were fixed at 0.2 m. The *RRMSE*s between the GPR-derived ISM values and the corresponding augering measurements were all lower than 22.2%, whereas *RMSEs* were lower than 0.017 $m^3 \cdot m^{-3}$, regardless of the study plot and soil depth (Figures 10c, 10f, 10i, 10l and 11c, 11f, 11i), indicating a good estimation accuracy of ISM by the proposed method.

Soil depth influenced the accuracy of the ISM estimates. In Plot 1, the correlation coefficient between ISM estimates and augering measurements was much lower in the near-surface soil layer (0.0–0.2 m depth) than in the subsoil (0.2–0.4, 0.4–0.6, and 0.6–0.8 m depths). In Plot 2, the deepest investigated soil layer (0.5–0.7 m depth) showed a lower correlation coefficient between ISM estimates and augering measurements than did the shallower layers (0.1–0.3 and 0.3–0.5 m depth). The apparent dependence of the accuracy of ISM estimates on soil depth was also likely related to the vertical distribution of PSWS scatters (Figure 7), which determined the accuracy of the estimation of PSWS (Figures 8 and 9).

In addition to the good accuracy in terms of absolute values, the GPR-derived 2D distributions of ISM closely resembled the spatial variation suggested by the augering data (Figures 10 and 11). With exceptions of the soil layers of 0.2–0.4 m in Plot 1 and 0.5–0.7 m in Plot 2, where the GPR results overestimated the ISM obtained by augering, the GPR estimation and augering measurements were distributed along both sides of the 1:1 line. Moreover, the general patterns of the transition from relatively wet spots to dry spots at each investigated depth were very similar between the GPR results and augering results.

5.3. Three-Dimensional Visualization of RZSM

The 3D visualizations of ISM for both plots, as generated by the proposed GPR method, were illustrated in Figure 12. The RZSM in Plot 1 showed an overall increase with soil depth (Figures 12a–12c), whereas the general trend of RZSM against soil depth was not noticeable in Plot 2 (Figures 12e and 12f). The spatial variability of RZSM at different soil depths between two study plots was compared in Figure 13. In line with the higher degree of the heterogeneity of 3D distribution of RZSM in Plot 2 than Plot 1 visually (Figure 12), the value of *STD* of RZSM in Plot 2 was greater than that in Plot 1 overall. Moreover, the *STD*s of RZSM in both Plot 1 and Plot 2 presented a unimodal distribution against soil depth and peaked around 0.5 m depth, which agreed with the root distribution in study plots (Figure S5).

6. Discussion

6.1. Advantages of the Proposed Method in Characterizing RZSM

The method established in this study extends the FO reflected wave method to determine the 2D and 3D distributions of RZSM noninvasively. First, instead of burying reflectors in the root zone as required by the traditional applications of the FO reflected wave method (e.g., Lunt et al., 2005), coarse roots are employed as natural reflectors in the proposed method, making this method truly noninvasive and, thus, repeatable. The wide distribution of coarse roots through the root zone (e.g., Figure 7) is favorable for the proposed method to quantify and map RZSM in both 2D and 3D. Second, the proposed method adopts the automatic hyperbola identification algorithm to estimate GPR wave velocities from numerous coarse root reflections in GPR images (Figure 3), which has been proven efficient and accurate and allows GPR-based root detection at larger areas (Li et al., 2016; Liu, Cui, et al., 2019). Therefore, the proposed method greatly boosts the speed of mapping soil moisture of the field scale compared with traditional methods, such as the point-based measurements by augering and drying soil samples in the lab.

The proposed method characterizes RZSM of the deep subsoil, for example, up to 0.9 m deep in this study (Figure 12), whereas previous GPR-based methods commonly obtain the average soil moisture only to the depth of 0.2 m (e.g., Qin et al., 2013; Weihermüller et al., 2007; Wu et al., 2019). The proposed method is effective in quantifying RZSM to the depth of the deepest coarse roots that can be detected in GPR images. In addition, through comparing the difference in PSWS at two different soil

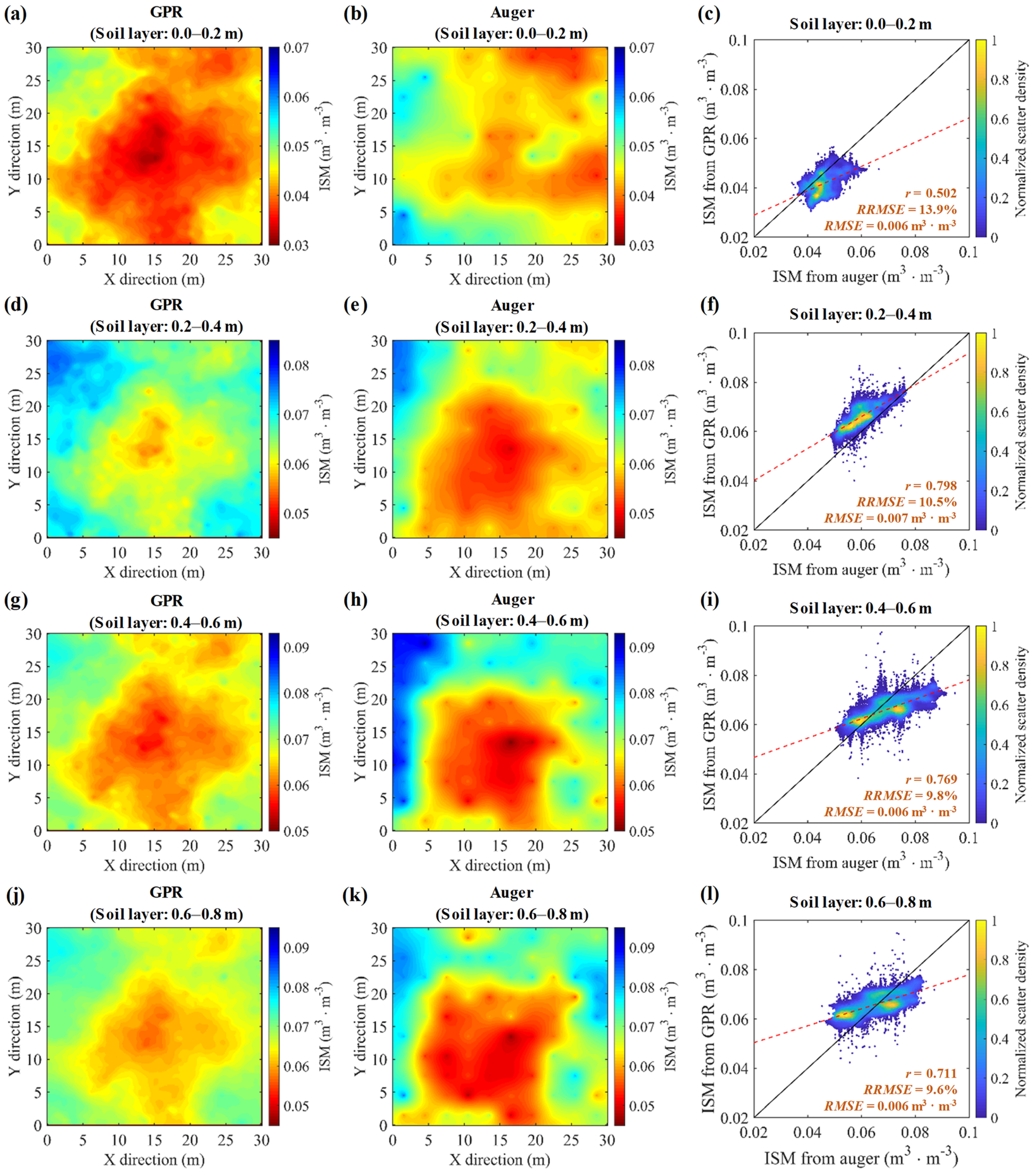

Figure 10. Comparisons of ISM distributions estimated from the GPR method (a,d,g,j) and auger sampling (b,e,h,k) for different soil layers in Plot 1. (c,f,i,l) Density scatter plots of ISMs estimated from GPR and augers for soil layers of 0–0.2, 0.2–0.4, 0.4–0.6, and 0.6–0.8 m, respectively. The red dashed line indicates the linear regression model between estimates from GPR and measurements from augering. The black line is the 1:1 relationship. The color bar indicates the density of scatters.

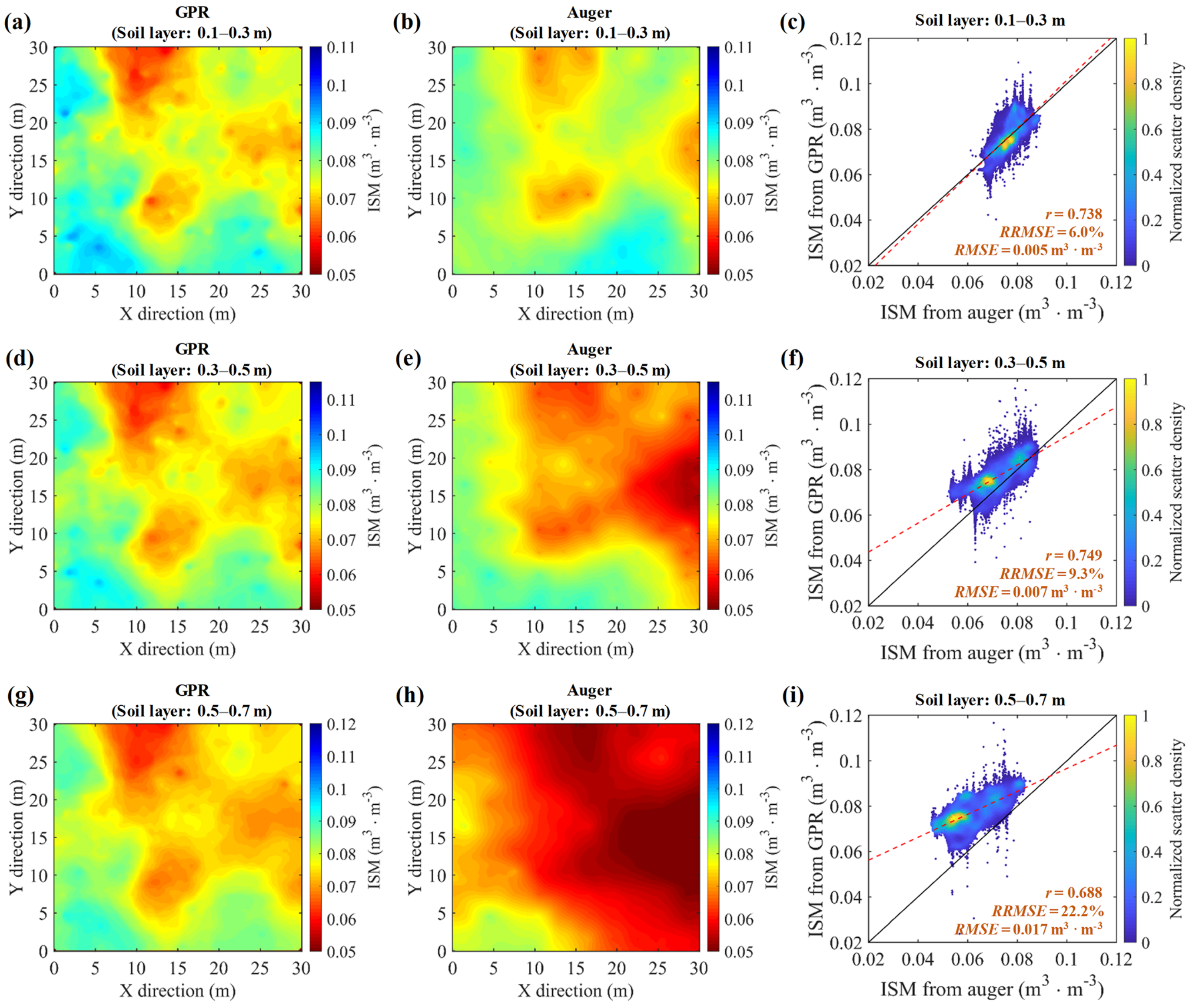

Figure 11. Comparisons of ISM distributions estimated from the GPR method (a,d,g) and auger sampling (b,e,h) for different soil layers in Plot 2. (c,f,i) Density scatter plot of ISMs estimated from GPR and augers for soil layers of 0.1–0.3, 0.3–0.5, and 0.5–0.7 m, respectively. The red dashed line indicates the linear regression model between estimates from GPR and measurements from augering. The black line is the 1:1 relationship. The color bar indicates the density of scatters.

depths (equations 11 and 12), the proposed method captures the variation of soil moisture along the depth, which extends the application of GPR to map the 2D distribution of surface soil moisture to the 3D distribution of RZSM (e.g., Figure 12).

In recent years, GPR has been successfully adopted in many field root studies (Guo et al., 2013a). The proposed method further enhances the application of GPR in studying roots in the field by simultaneously providing information on the distribution patterns of coarse roots, PSWS, and ISM (e.g., Figures 8–11). As the traditional method of measuring PSWS is via invasive sampling of ASM at different soil depths (e.g., Liu & Shao, 2014), the proposed method provides a noninvasive way to determine PSWS, which allows repeated monitoring.

To the best of our knowledge, this is the first study using ground-coupled GPR with a fixed-offset antenna configuration to examine the 2D and 3D distributions of RZSM. The ground-coupled GPR with a

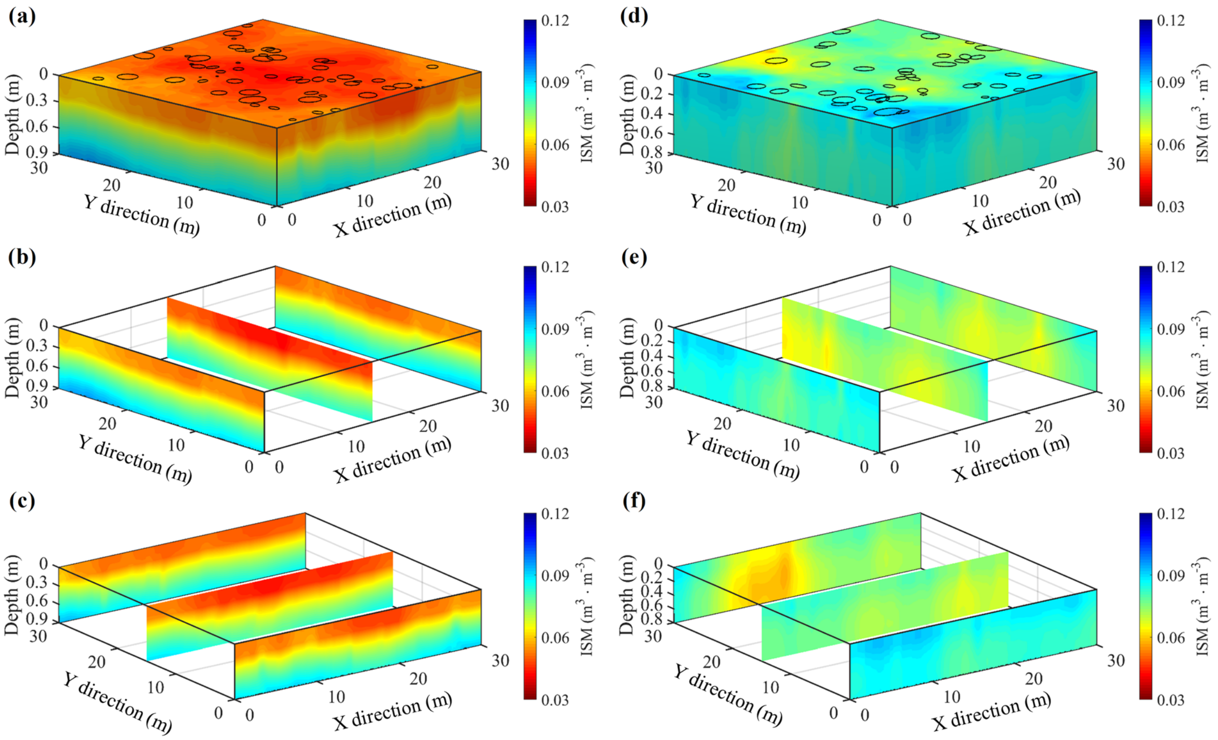

Figure 12. The 3D visualization of RZSM estimated by GPR for Plot 1 (a–c) and Plot 2 (d–f), respectively. Open ovals on the surface indicate the distribution and size of shrub canopies.

fixed-offset antenna configuration is the most popular commercial GPR because of its easy operation and rapid data collection (Jol, 2009). However, only a few efforts have been pursued to test and refine the application of the GPR-FO configuration in the noninvasive mapping of subsoil moisture (e.g., Huisman et al., 2003; Liu, Chen, et al., 2019; Liu, Cui, et al., 2019). The proposed method establishes a standard protocol to work with the GPR-FO configuration to map soil moisture down to the deep root zone.

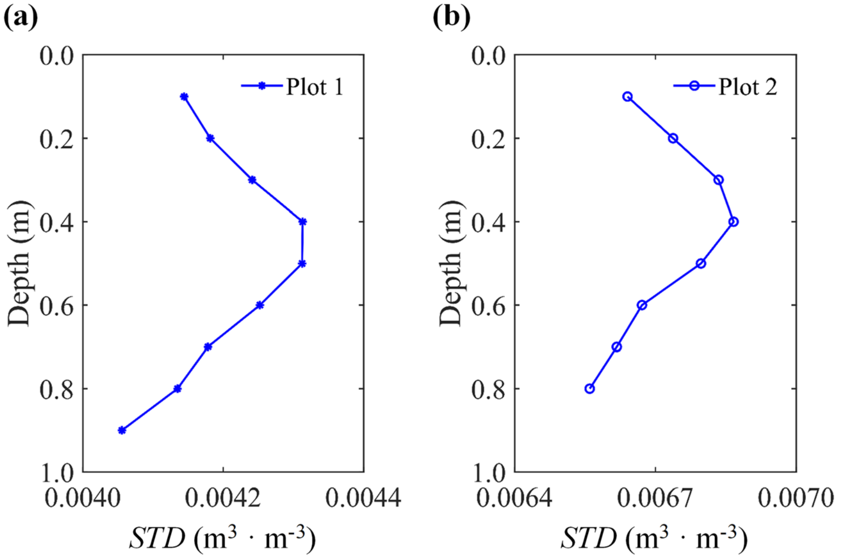

Figure 13. The standard deviation (*STD*) of soil moisture at a certain depth is compared between Plot 1 (a) and Plot 2 (b) in the root zone. Data used to calculate the *STD* of soil moisture are from the 3D RZSM estimated by GPR (i.e., Figure 12).

6.2. Uncertainties and Possible Improvements of the Proposed Method

The presence of coarse roots is the prerequisite for the proposed method. The number and distribution of coarse roots, as well as the factors influencing GPR-based root detection, can introduce uncertainties during the application of the proposed method in the field.

First, root parameters, for example, gravimetric water content, diameter, depth, and interval length (Hirano et al., 2009), soil conditions, for example, soil moisture content, soil texture, and heterogeneity in soil structures (Butnor et al., 2001; Dannoura et al., 2008), the antenna frequency of a GPR system (Hirano et al., 2012), and the layout of survey lines or the relative position of root branching direction and survey line direction (Guo et al., 2015; Tanikawa et al., 2013) all possibly influence the efficiency of GPR to detect coarse roots and the quality of coarse root reflections in GPR images. Coarse root reflections with poor quality, such as low signal-to-noise ratio, incomplete hyperbolic shape, signal interference, and noise clutter, can impair the performance of the automatic identification of hyperbola reflections in GPR images (Li et al., 2016) and further decrease the accuracy of the estimation of GPR wave velocity and soil moisture.

Second, the number and distribution of identified coarse roots determine the performance of the spatial interpolation of PSWS scatters to the 2D and 3D RZSM (Li et al., 2014; Lu & Wong, 2008; Zhang & Shao, 2015). The distribution pattern of PSWS scatters affects the fitting of a proper trend model (Figure S3), which also introduces uncertainty into the generation of the 2D distributions of PSWS. As shown in Figures 7, 8, and 9, the 2D distribution of the PSWS estimates had the highest accuracy at the soil depths with the most abundant PSWS scatters (i.e., 0.4 m and 0.6 m in Plot 1 and 0.5 m in Plot 2). Insufficient PSWS scatters at soil depths of approximately 0.3 and 0.7 m in Plot 2 led to a larger bias in the estimation of PSWS (Figures 9c, 9f, and 9i). Moreover, due to the generally more abundant number of PSWS scatters along the soil depth, the PSWS estimates in Plot 1 had a higher accuracy with augering data than Plot 2 (Figures 8 and 9). In addition, the lower estimation accuracy of soil moisture in the shallow subsurface, <0.2 m depth in Plot 1 and <0.3 m depth in Plot 2 (Figures 8c and 9c), could be attributed to the joint influences of inadequate PSWS scatters and surface conditions.

Third, the uncertainty in ISM estimates might be attributed to errors in PSWS distribution, which could be transferred by equations (11) and (12). As shown in Figures 10c and 11c, the GPR-based ISM distribution for 0.0–0.2 m soil layer had a lower correlation coefficient than that for other soil layers in Plot 1, which was consistent with the results of the PSWS estimation (Figure 8c). The ISM distribution for the soil layer of 0.5–0.7 m in Plot 2 had a relatively high *RRMSE* due to the overestimate for PSWS distribution at a soil depth of 0.7 m (Figure 9i). Therefore, the performance of PSWS estimation could further affect the ISM estimation through equations (11) and (12).

Although results of this study validated the effectiveness of the proposed method in shrubland with dry sandy soils and extensive lateral coarse roots, its performance should be tested in different environments in the future. Thus far, successful applications of GPR-based root detection and quantification have been reported in various biomes, such as the subtropical evergreen broad-leaved forest in south China (Yan et al., 2013), conifer forest with sandy soil in coastal regions in Japan (Hirano et al., 2012), agroforestry systems with sandy loam in Africa (Isaac et al., 2014), oak-grass savanna in the west coast of the United States (Raz-Yaseef et al., 2013), pine plantation on sandy soil in the east coast of the United States (Butnor et al., 2001), shrubs in semiarid region in north China (Cui et al., 2020), and street trees on anthropogenic soil under urban settings (Altdorff et al., 2019). These conditions and species can be chosen to further test the proposed method. However, given the limiting factors of GPR-based root investigation that are discussed above, soils with high clay or water content and at sites with rolling topography, which is the case for most forests, the efficiency of the proposed method is likely low. Under ideal soil and site conditions, such as the shrubland studied here with abundant lateral roots distributing in dry sandy soil and flat terrain, the proposed method can be most effective for augmenting traditional soil moisture sampling.

In the future, the proposed method can be further improved in the following aspects. First, the linear trend model of PSWS used in this study (equation 6) can be replaced by more sophisticated models (e.g., higher-degree polynomial or exponential models), or combined with hydrological process models (e.g., Hydrus models; Tran et al., 2014), to better characterize the variation of PSWS with soil depth in environments with heterogeneous soil conditions. Second, this study employed the IDW method for spatial interpolation due to its efficiency in computation and less requirement of additional parameters. Other more sophisticated interpolation methods, for example, spatio-temporal Kriging (Jost et al., 2005; Yang et al., 2015), can be tested to further improve the overall performance of the proposed method. Third, while the current method only depends on the hyperbolic reflections of coarse roots, other buried objects (e.g., small rocks) can also be tested as reflectors, which also form hyperbolic reflections in GPR images (Guo et al., 2013a), to implement the proposed methods in different soil landscapes. With continuous improvements in GPR system hardware (Lualdi & Lombardi, 2014; Sagnard & Tebchrany, 2015), data collection with nonperpendicular survey line setups (Guo et al., 2015), and the automatic hyperbola identification algorithm, for example, based on machine learning (Lei et al., 2019; Maas & Schmalzl, 2013), we believe that the application range of the proposed method and other applications of GPR-based root investigation can be further extended to more environments.

6.3. Potential Applications of the Proposed Method in Ecohydrological Studies

In follow-up studies, we will take advantage of the proposed method of the simultaneous measurements for coarse roots, PSWS, and ISM to explore the interplay between coarse roots and soil moisture as well as the subsurface ecohydrological processes in shrublands under shrub encroachment (Cao et al., 2018, 2019; Li, Zhang, et al., 2013). For example, results in both plots of this study revealed a negative relationship between PSWS and the distribution density of shrub canopies (Figures 8 and 9); that is, the higher shrub density above-ground was associated with lower PSWS below-ground. Such a correspondence between above- and below-ground likely indicates the impact of vegetation transpiration on the spatial variation of soil water distribution (Guswa et al., 2002). However, previous studies frequently found that subcanopy soils are moister than intercanopy areas, which facilitate shrub seedling establishment and growth beneath the canopy (e.g., D'Odorico et al., 2007).

Moreover, the discrepancies of RZSM distribution between plots can be explained by different distribution patterns of both canopies and roots (Figure 7), microtopography, as well as meteorological conditions at different experiment dates (12 July 2017 for Plot 1 and 17 August 2018 for Plot 2). Because the growing season at the study site is winding down in August, the shrubs consume less soil water than they do in July, and the higher evapotranspiration rate in July results in drier soil in the shallow subsurface. The joint influence of microtopography and meteorological conditions make the surface soil moisture in Plot 2 display more variations (Figure 12). It will be interesting to repeat GPR surveys for the same plot in different seasons to investigate the temporal stability of the spatial pattern of RZSM as well as the reproducibility of the proposed method under different meteorological conditions. A recent study conducted in the same region indicated that the winter condition is more favorable for GPR-based root detection, with more roots identified in the deeper subsoil (Cui et al., 2020). Therefore, at the study site, the maximum depth of measuring RZSM by the proposed method can be further extended to the deeper in winter. The consistency between the *STD* of RZSM and the number of coarse roots demonstrates the process that a shrub root system amplifies the heterogeneity in the spatial distribution of soil water (Figures 13 and S5). Therefore, the proposed method can be used to explore the complex interactions between root and soil water and link the above-ground large-scale patterns derived from remotely sensed data to the below-ground ecohydrological processes.

Recent studies have noted the significance of GPR data assimilation in improving the accuracy of hydrodynamic model predictions and hydraulic parameter estimation (Robinson, Binley, et al., 2008; Tran et al., 2014). Determining the best way to assimilate field RZSM distributions estimated with our proposed method into soil hydrodynamic model will contribute to obtaining accurate spatiotemporal variability and responses of hydraulic parameters to climate changes, which facilitates the related studies of agriculture water management.

7. Conclusions

This study employed coarse root reflections collected by GPR-FO to estimate 2D and 3D distributions of RZSM in a noninvasive manner. The proposed method was tested in two field shrub plots (each of 900 m^2) with different distribution densities of coarse roots. Compared with soil moisture measurement of augered soil samples, the 2D distributions of RZSM derived from GPR achieved *RMSE* values less than

0.017 $m^3 \cdot m^{-3}$ (even 0.010 $m^3 \cdot m^{-3}$ in most cases) and correlation coefficients from 0.502 to 0.798 for diverse soil layers in both plots. The 3D visualization of RZSM revealed the spatial variation of RZSM for 0 to 0.9 m depths. The superior performance of our GPR-based method demonstrated the feasibility of its use for the 2D and 3D visualization of RZSM. Given the increasing accessibility of GPR field data, we expect broader applications of our method to enhance the understanding of the complex plant-soil-water interactions by providing accurate information about the distributions of roots and soil moisture without destroying the soil environment.

Acknowledgments
The GPR raw data and the soil moisture data obtained by augering will be archived in ZENODO (www.zenodo.org). The authors are thankful for the assistance in field data collection from Qixin Liu, Zhenxian Quan, Qi Dong, Chishan Zhang, and Wenqing Wang. Financial support was provided by the National Natural Science Foundation of China (Grants 41571404 and 51879172). The source codes of GPR data processing, spatial interpolation, and data visualization are available from the authors upon request (lug163@psu.edu or guolistory@gmail.com). We are also thankful for the Editor (D. Scott Mackay), the Associate Editor (J.A. (Sander) Huisman), and three anonymous reviewers for their suggestions that have helped greatly improve the quality of this paper.

References

Allroggen, N., van Schaik, N. L. M. B., & Tronicke, J. (2015). 4D ground-penetrating radar during a plot scale dye tracer experiment. *Journal of Applied Geophysics*, *118*, 139–144. https://doi.org/10.1016/j.jappgeo.2015.04.016

Altdorff, D., Botschek, J., Honds, M., van der Kruk, J., & Vereecken, H. (2019). In situ detection of tree root systems under heterogeneous anthropogenic soil conditions using ground penetrating radar. *Journal of Infrastructure Systems*, *25*(3), 05019008. https://doi.org/10.1061/(ASCE)IS.1943-555X.0000501

Asbjornsen, H., Goldsmith, G. R., Alvarado-Barrientos, M. S., Rebel, K., Van Osch, F. P., Rietkerk, M., et al. (2011). Ecohydrological advances and applications in plant-water relations research: A review. *Journal of Plant Ecology*, *4*(1-2), 3–22. https://doi.org/10.1093/jpe/rtr005

Babaeian, E., Sadeghi, M., Jones, S. B., Montzka, C., Vereecken, H., & Tuller, M. (2019). Ground, proximal and satellite remote sensing of soil moisture. *Reviews of Geophysics*, *57*(2), 530–616. https://doi.org/10.1029/2018RG000618

Baldwin, D., Manfreda, S., Keller, K., & Smithwick, E. A. H. (2017). Predicting root zone soil moisture with soil properties and satellite near-surface moisture data across the conterminous United States. *Journal of Hydrology*, *546*, 393–404. https://doi.org/10.1016/J.JHYDROL.2017.01.020

Benedetto, A., Tosti, F., Bianchini Ciampoli, L., & D'Amico, F. (2017). An overview of ground-penetrating radar signal processing techniques for road inspections. *Signal Processing*, *132*, 201–209. https://doi.org/10.1016/j.sigpro.2016.05.016

Butnor, J. R., Doolittle, J. A., Johnsen, K. H., Samuelson, L., Stokes, T., & Kress, L. (2003). Utility of ground-penetrating radar as a root biomass survey tool in forest systems. *Soil Science Society of America Journal*, *67*(5), 1607–1615. https://doi.org/10.2136/sssaj2003.1607

Butnor, J. R., Doolittle, J. A., Kress, L., Cohen, S., & Johnsen, K. H. (2001). Use of ground-penetrating radar to study tree roots in the southeastern United States. *Tree Physiology*, *21*(17), 1269–1278. https://doi.org/10.1093/treephs/21.17.1269

Cao, X., Liu, Y., Cui, X., Chen, J., & Chen, X. (2019). Mechanisms, monitoring and modeling of shrub encroachment into grassland: A review. *International Journal of Digital Earth*, *12*(6), 625–641. https://doi.org/10.1080/17538947.2018.1478004

Cao, X., Liu, Y., Liu, Q., Cui, X., Chen, X., & Chen, J. (2018). Estimating the age and population structure of encroaching shrubs in arid/semiarid grasslands using high spatial resolution remote sensing imagery. *Remote Sensing of Environment*, *216*, 572–585. https://doi.org/10.1016/j.rse.2018.07.025

Chi, D., Wang, H., Li, X., Liu, H., & Li, X. (2018). Assessing the effects of grazing on variations of vegetation NPP in the Xilingol Grassland, China, using a grazing pressure index. *Ecological Indicators*, *88*, 372–383. https://doi.org/10.1016/J.ECOLIND.2018.01.051

Cho, E., Choi, M., & Wagner, W. (2015). An assessment of remotely sensed surface and root zone soil moisture through active and passive sensors in northeast Asia. *Remote Sensing of Environment*, *160*, 166–179. https://doi.org/10.1016/J.RSE.2015.01.013

Collins, D. B. G., & Bras, R. L. (2007). Plant rooting strategies in water-limited ecosystems. *Water Recourses Research*, *43*, 1–10. https://doi.org/10.1029/2006WR005541

Cui, X., Guo, L., Chen, J., Chen, X., & Zhu, X. (2013). Estimating tree-root biomass in different depths using ground-penetrating radar: Evidence from a controlled experiment. *IEEE Transactions on Geoscience and Remote Sensing*, *51*, 3410–3423. https://doi.org/10.1109/TGRS.2012.2224351

Cui, X., Liu, X., Cao, X., Fan, B., Zhang, Z., Chen, J., et al. (2020). Pairing dual-frequency GPR in summer and winter enhances the detection and mapping of coarse roots in the semi-arid shrubland in China. *European Journal of Soil Science*, *71*(2), 236–251. https://doi.org/10.1111/ejss.12858

Daly, E., Porporato, A., Rodriguez-Iturbe, I., Daly, E., Porporato, A., & Rodriguez-Iturbe, I. (2004). Coupled dynamics of photosynthesis, transpiration, and soil water balance. Part I: Upscaling from hourly to daily level. *Journal of Hydrometeorology*, *5*, 546–558. https://doi.org/10.1175/1525-7541(2004)005<0546:CDOPTA>2.0.CO;2

Dannoura, M., Hirano, Y., Igarashi, T., Ishii, M., Aono, K., Yamase, K., & Kanazawa, Y. (2008). Detection of *Cryptomeria japonica* roots with ground penetrating radar. *Plant Biosystems*, *142*(2), 375–380. https://doi.org/10.1080/11263500802150951

Das, N. N., Entekhabi, D., Dunbar, R. S., Colliander, A., Chen, F., Crow, W., et al. (2018). The SMAP mission combined active-passive soil moisture product at 9 km and 3 km spatial resolutions. *Remote Sensing of Environment*, *211*, 204–217. https://doi.org/10.1016/J.RSE.2018.04.011

Das, N. N., Mohanty, B. P., Cosh, M. H., & Jackson, T. J. (2008). Modeling and assimilation of root zone soil moisture using remote sensing observations in Walnut Gulch Watershed during SMEX04. *Remote Sensing of Environment*, *112*(2), 415–429. https://doi.org/10.1016/J.RSE.2006.10.027

Dim, J. R., & Takamura, T. (2013). Alternative approach for satellite cloud classification: Edge gradient application. *Advances in Meteorology*, *2013*, 1–8. https://doi.org/10.1155/2013/584816

D'Odorico, P., Caylor, K., Okin, G. S., & Scanlon, T. M. (2007). On soil moisture-vegetation feedbacks and their possible effects on the dynamics of dryland ecosystems. *Journal of Geophysical Research – Biogeosciences*, *112*(G4), G04010. https://doi.org/10.1029/2006JG000379

Ford, T. W., Harris, E., & Quiring, S. M. (2014). Estimating root zone soil moisture using near-surface observations from SMOS. *Hydrology and Earth System Sciences*, *18*(1), 139–154. https://doi.org/10.5194/hess-18-139-2014

Grote, K., Hubbard, S., & Rubin, Y. (2002). GPR monitoring of volumetric water content in soils applied to highway construction and maintenance. *The Leading Edge*, *21*(5), 482–504. https://doi.org/10.1190/1.1481259

Guo, L., Chen, J., Cui, X., Fan, B., & Lin, H. (2013). Application of ground penetrating radar for coarse root detection and quantification: A review. *Plant and Soil*, *362*, 1–23. https://doi.org/10.1007/s11104-012-1455-5

Guo, L., & Lin, H. (2016). Critical Zone research and observatories: Current status and future perspectives. *Vadose Zone Journal*, *15*, 1–14. https://doi.org/10.2136/vzj2016.06.0050

Guo, L., & Lin, H. (2018). Addressing two bottlenecks to advance the understanding of preferential flow in soils. *Advances in Agronomy*, *147*, 61–117. https://doi.org/10.1016/BS.AGRON.2017.10.002

Guo, L., Lin, H., Fan, B., Cui, X., & Chen, J. (2013b). Impact of root water content on root biomass estimation using ground penetrating radar: Evidence from forward simulations and field controlled experiments. *Plant and Soil*, *371*, 503–520. https://doi.org/10.1007/s11104-013-1710-4

Guo, L., Lin, H., Fan, B., Cui, X., & Chen, J. (2013c). Forward simulation of root's ground penetrating radar signal: Simulator development and validation. *Plant and Soil*, *372*(1-2), 487–505. https://doi.org/10.1007/s11104-013-1751-8

Guo, L., Wu, Y., Chen, J., Hirano, Y., Tanikawa, T., Li, W., & Cui, X. (2015). Calibrating the impact of root orientation on root quantification using ground-penetrating radar. *Plant and Soil*, *395*(1-2), 289–305. https://doi.org/10.1007/s11104-015-2563-9

Guswa, A. J., Celia, M. A., & Rodriguez-Iturbe, I. (2002). Models of soil moisture dynamics in ecohydrology: A comparative study. *Water Resources Research*, *38*, 5-1–5-15. https://doi.org/10.1029/2001WR000826

He, B., Wang, S. R., Guo, L. L., & Wu, X. C. (2019). Aridity change and its correlation with greening over drylands. *Agricultural and Forest Meteorology*, *278*, 1–9. https://doi.org/10.1016/j.agrformet.2019.107663

Hirano, Y., Dannoura, M., Aono, K., Igarashi, T., Ishii, M., Yamase, K., et al. (2009). Limiting factors in the detection of tree roots using ground-penetrating radar. *Plant and Soil*, *319*(1-2), 15–24. https://doi.org/10.1007/s11104-008-9845-4

Hirano, Y., Yamamoto, R., Dannoura, M., Aono, K., Igarashi, T., Ishii, M., et al. (2012). Detection frequency of *Pinus thunbergii* roots by ground-penetrating radar is related to root biomass. *Plant and Soil*, *360*(1-2), 363–373. https://doi.org/10.1007/s11104-012-1252-1

Hruška, J., Cermák, J., & Sustek, S. (1999). Mapping tree root systems with ground-penetrating radar. *Tree Physiology*, *19*(2), 125–130. https://doi.org/10.1093/treephys/19.2.125

Huang, L., He, B., Han, L., Liu, J. J., Wang, H. Y., & Chen, Z. Y. (2017). A global examination of the response of ecosystem water-use efficiency to drought based on MODIS data. *Science of the Total Environment*, *601*, 1097–1107. https://10.1016/j.scitotenv.2017.05.084

Huisman, J. A., Hubbard, S. S., Redman, J. D., & Annan, A. P. (2003). Measuring soil water content with ground penetrating radar: A review. *Vadose Zone Journal*, *2*, 476–491. https://doi.org/10.2113/2.4.476

Huisman, J. A., Snepvangers, J., Bouten, W., & Heuvelink, G. (2002). Mapping spatial variation in surface soil water content: Comparison of ground-penetrating radar and time domain reflectometry. *Journal of Hydrology*, *269*, 194–207. https://doi.org/10.1016/s0022-1694(02)00239-1

Isaac, M. E., Anglaaere, L. C. N., Borden, K., & Adu-Bredu, S. (2014). Intraspecific root plasticity in agroforestry systems across edaphic conditions. *Agriculture, Ecosystems and Environment*, *185*, 16–23. https://doi.org/10.1016/j.agee.2013.12.004

Jol, H. M. (2009). *Ground penetrating radar theory and applications*. Amsterdam: Elsevier.

Jonard, F., André, F., Ponette, Q., Vincke, C., & Jonard, M. (2011). Sap flux density and stomatal conductance of European beech and common oak trees in pure and mixed stands during the summer drought of 2003. *Journal of Hydrology*, *409*, 371–381. https://doi.org/10.1016/J.JHYDROL.2011.08.032

Jonard, F., Bogena, H., Caterina, D., Garré, S., Klotzsche, A., Monerris, A., et al. (2017). Ground-based soil moisture determination. In X. Li, & H. Vereecken (Eds.), *Observation and measurement*, (pp. 1–42). Berlin, Heidelberg: Springer. https://doi.org/10.1007/978-3-662-47871-4_2-1

Jost, G., Heuvelink, G. B. M., & Papritz, A. (2005). Analysing the space–time distribution of soil water storage of a forest ecosystem using spatio-temporal kriging. *Geoderma*, *128*, 258–273. https://doi.org/10.1016/J.GEODERMA.2005.04.008

Klotzsche, A., Jonard, F., Looms, M. C., van der Kruk, J., & Huisman, J. A. (2018). Measuring soil water content with ground penetrating radar: A decade of progress. *Vadose Zone Journal*, *17*, 1–9. https://doi.org/10.2136/vzj2018.03.0052

Lei, W., Hou, F., Xi, J., Tan, Q., Xu, M., Jiang, X., et al. (2019). Automatic hyperbola detection and fitting in GPR B-scan image. *Automation in Construction*, *106*, 102839. https://doi.org/10.1016/j.autcon.2019.102839

Li, L., Losser, T., Yorke, C., & Piltner, R. (2014). Fast inverse distance weighting-based spatiotemporal interpolation: A web-based application of interpolating daily fine particulate matter $PM_{2.5}$ in the contiguous U.S. using parallel programming and k-d tree. *International Journal of Environmental Research and Public Health*, *11*(9), 9101–9141. https://doi.org/10.3390/ijerph110909101

Li, W., Cui, X., Guo, L., Chen, J., Chen, X., & Cao, X. (2016). Tree root automatic recognition in ground penetrating radar profiles based on randomized Hough transform. *Remote Sensing*, *8*(5), 1, 430–16. https://doi.org/10.3390/rs8050430

Li, X., Zhang, S., Peng, H., Hu, X., & Ma, Y. (2013). Soil water and temperature dynamics in shrub-encroached grasslands and climatic implications: Results from Inner Mongolia steppe ecosystem of north China. *Agricultural and Forest Meteorology*, *171-172*, 20–30. https://doi.org/10.1016/j.agrformet.2012.11.001

Li, Z., Tang, B., Wu, H., Ren, H., Yan, G., Wan, Z., et al. (2013). Satellite-derived land surface temperature: Current status and perspectives. *Remote Sensing of Environment*, *131*, 14–37. https://doi.org/10.1016/J.RSE.2012.12.008

Liu, B., & Shao, M. (2014). Estimation of soil water storage using temporal stability in four land uses over 10 years on the Loess Plateau, China. *Journal of Hydrology*, *517*, 974–984. https://doi.org/10.1016/J.JHYDROL.2014.06.003

Liu, X., Chen, J., Cui, X., Liu, Q., Cao, X., & Chen, X. (2019). Measurement of soil water content using ground-penetrating radar: A review of current methods. *International Journal of Digital Earth*, *12*(1), 95–118. https://doi.org/10.1080/17538947.2017.1412520

Liu, X., Cui, X., Guo, L., Chen, J., Li, W., Yang, D., et al. (2019). Non-invasive estimation of root zone soil moisture from coarse root reflections in ground-penetrating radar images. *Plant and Soil*, *436*(1-2), 623–639. https://doi.org/10.1007/s11104-018-03919-5

Lu, G., & Wong, D. (2008). An adaptive inverse-distance weighting spatial interpolation technique. *Computers & Geosciences*, *34*(9), 1044–1055. https://doi.org/10.1016/J.CAGEO.2007.07.010

Lualdi, M., & Lombardi, F. (2014). Combining orthogonal polarization for elongated target detection with GPR. *Journal of Geophysics and Engineering*, *11*(5), 055006. https://doi.org/10.1088/1742-2132/11/5/055006

Lunt, I. A., Hubbard, S. S., & Rubin, Y. (2005). Soil moisture content estimation using ground-penetrating radar reflection data. *Journal of Hydrology*, *307*(1-4), 254–269. https://doi.org/10.1016/J.JHYDROL.2004.10.014

Maas, C., & Schmalzl, J. (2013). Using pattern recognition to automatically localize reflection hyperbolas in data from ground penetrating radar. *Computers and Geosciences*, *58*, 116–125. https://doi.org/10.1016/j.cageo.2013.04.012

Molon, M., Boyce, J. I., & Arain, M. A. (2017). Quantitative, nondestructive estimates of coarse root biomass in a temperate pine forest using 3-D ground-penetrating radar (GPR). *Journal of Geophysical Research – Biogeosciences*, *122*, 80–102. https://doi.org/10.1002/2016JG003518

Parsekian, A. D., Singha, K., Minsley, B. J., Holbrook, W. S., & Slater, L. (2015). Multiscale geophysical imaging of the critical zone. *Reviews of Geophysics*, *53*, 1–26. https://doi.org/10.1002/2014RG000465

Peng, J., Loew, A., Merlin, O., & Verhoest, N. E. C. (2017). A review of spatial downscaling of satellite remotely sensed soil moisture. *Reviews of Geophysics*, *55*, 341–366. https://doi.org/10.1002/2016RG000543

Petropoulos, G. P., Griffiths, H. M., Dorigo, W., Xaver, A., & Gruber, A. (2013). Surface soil moisture estimation: Significance, controls and conventional measurement techniques. In G. P. Petropoulos (Ed.), *Remote sensing of energy fluxes and soil moisture content* (pp. 29–48). Boca Raton, FL, USA: Taylor and Francis.

Polak, A., & Wallach, R. (2001). Analysis of soil moisture variations in an irrigated orchard root zone. *Plant and Soil*, *233*, 145–159. https://doi.org/10.1023/A:1010351101314

Qin, Y., Chen, X., Zhou, K., Klenk, P., Roth, K., & Sun, L. (2013). Ground-penetrating radar for monitoring the distribution of near-surface soil water content in the Gurbantünggüt Desert. *Environmental Earth Sciences*, *70*(6), 2883–2893. https://doi.org/10.1007/s12665-013-2528-3

Raffelli, G., Previati, M., Canone, D., Gisolo, D., Bevilacqua, I., Capello, G., et al. (2017). Local- and plot-scale measurements of soil moisture: Time and spatially resolved field techniques in plain, hill and mountain sites. *Watermark*, *9*(9), 706. https://doi.org/10.3390/w9090706

Raz-Yaseef, N., Koteen, L., & Baldocchi, D. D. (2013). Coarse root distribution of a semi-arid oak savanna estimated with ground penetrating radar. *Journal of Geophysical Research – Biogeosciences*, *118*(1), 135–147. https://doi.org/10.1029/2012JG002160

Reynolds, J. M. (1997). *An introduction to applied and environmental geophysics*. Chichester: John Wiley & Sons.

Rial, F. I., Pereira, M., Lorenzo, H., Arias, P., & Novo, A. (2009). Resolution of GPR bowtie antennas: An experimental approach. *Journal of Applied Geophysics*, *67*(4), 367–373. https://doi.org/10.1016/J.JAPPGEO.2008.05.003

Robinson, D. A., Abdu, H., Lebron, I., & Jones, S. B. (2012). Imaging of hill-slope soil moisture wetting patterns in a semi-arid oak savanna catchment using time-lapse electromagnetic induction. *Journal of Hydrology*, *416-417*, 39–49. https://doi.org/10.1016/j.jhydrol.2011.11.034

Robinson, D. A., Binley, A., Crook, N., Day-Lewis, F. D., Ferré, T. P. A., Grauch, V. J. S., et al. (2008). Advancing process-based watershed hydrological research using near-surface geophysics: A vision for, and review of, electrical and magnetic geophysical methods. *Hydrological Processes*, *22*(18), 3604–3635. https://doi.org/10.1002/hyp.6963

Robinson, D. A., Campbell, C. S., Hopmans, J. W., Hornbuckle, B. K., Jones, S. B., Knight, R., et al. (2008). Soil moisture measurement for ecological and hydrological watershed-scale observatories: A review. *Vadose Zone Journal*, *7*(1), 358–389. https://doi.org/10.2136/vzj2007.0143

Sagnard, F., & Tebchrany, E. (2015). Using polarization diversity in the detection of small discontinuities by an ultra-wide band ground-penetrating radar. *Measurement: Journal of the International Measurement Confederation*, *61*, 129–141. https://doi.org/10.1016/j.measurement.2014.10.035

Seneviratne, S. I., Corti, T., Davin, E. L., Hirschi, M., Jaeger, E. B., Lehner, I., et al. (2010). Investigating soil moisture-climate interactions in a changing climate: A review. *Earth-Science Reviews*, *99*(3-4), 125–161. https://doi.org/10.1016/J.EARSCIREV.2010.02.004

Serbin, G., & Or, D. (2005). Ground-penetrating radar measurement of crop and surface water content dynamics. *Remote Sensing of Environment*, *96*(1), 119–134. https://doi.org/10.1016/j.rse.2005.01.018

Slob, E., Sato, M., & Olhoeft, G. (2010). Surface and borehole ground-penetrating-radar developments. *Geophysics*, *75*, 75A103–75A120. https://doi.org/10.1190/1.3480619

Snepvangers, J. J. J. C., Heuvelink, G., & B., M., Huisman, J. A. (2003). Soil water content interpolation using spatio-temporal kriging with external drift. *Geoderma*, *112*, 253–271. https://doi.org/10.1016/S0016-7061(02)00310-5

Sonkar, I., Kotnoor, H. P., & Sen, S. (2019). Estimation of root water uptake and soil hydraulic parameters from root zone soil moisture and deep percolation. *Agricultural Water Management*, *222*, 38–47. https://doi.org/10.1016/J.AGWAT.2019.05.037

Steelman, C. M., & Endres, A. L. (2012). Assessing vertical soil moisture dynamics using multi-frequency GPR common-midpoint soundings. *Journal of Hydrology*, *436–437*, 51–66. https://doi.org/10.1016/j.jhydrol.2012.02.041

Steelman, C. M., Endres, A. L., & Jones, J. P. (2012). High-resolution ground-penetrating radar monitoring of soil moisture dynamics: Field results, interpretation, and comparison with unsaturated flow model. *Water Resources Research*, *48*, 1–17. https://doi.org/10.1029/2011WR011414

Stoffregen, H., Zenker, T., & Wessolek, G. (2002). Accuracy of soil water content measurements using ground penetrating radar: Comparison of ground penetrating radar and lysimeter data. *Journal of Hydrology*, *267*, 201–206. https://doi.org/10.1016/S0022-1694(02)00150-6

Tanikawa, T., Hirano, Y., Dannoura, M., Yamase, K., Aono, K., Ishii, M., et al. (2013). Root orientation can affect detection accuracy of ground-penetrating radar. *Plant and Soil*, *373*(1-2), 317–327. https://doi.org/10.1007/s11104-013-1798-6

Topp, G. C., Davis, J. L., & Annan, A. P. (1980). Electromagnetic determination of soil water content: Measurements in coaxial transmission lines. *Water Recourses Research*, *16*(3), 574–582. https://doi.org/10.1029/WR016i003p00574

Tosti, F., & Slob, E. (2015). *Determination, by using GPR, of the volumetric water content in structures, substructures, foundations and soil (pp. 163–194)*. Cham: Springer. https://doi.org/10.1007/978-3-319-04813-0_7

Tran, A. P., Vanclooster, M., Zupanski, M., & Lambot, S. (2014). Joint estimation of soil moisture profile and hydraulic parameters by ground-penetrating radar data assimilation with maximum likelihood ensemble filter. *Water Recourses Research*, *50*, 3131–3146. https://doi.org/10.1002/2013WR014583

Vereecken, H., Huisman, J. A., Bogena, H., Vanderborght, J., Vrugt, J. A., & Hopmans, J. W. (2008). On the value of soil moisture measurements in vadose zone hydrology: A review. *Water Recourses Research*, *44*(4). https://doi.org/10.1029/2008WR006829

Vereecken, H., Huisman, J. A., Pachepsky, Y., Montzka, C., van der Kruk, J., Bogena, H., et al. (2014). On the spatio-temporal dynamics of soil moisture at the field scale. *Journal of Hydrology*, *516*, 76–96. https://doi.org/10.1016/J.JHYDROL.2013.11.061

Wang, Z., Hou, J., Qu, Z., Guo, J., & Li, J. (2017). Root distribution of 430 plants in temperate grassland of northern China. *Applied Ecology and Environmental Research*, *15*(3), 1625–1651. https://doi.org/10.15666/aeer/1503_16251651

Weihermüller, L., Huisman, J. A., Lambot, S., Herbst, M., & Vereecken, H. (2007). Mapping the spatial variation of soil water content at the field scale with different ground penetrating radar techniques. *Journal of Hydrology*, *340*(3-4), 205–216. https://doi.org/10.1016/j.jhydrol.2007.04.013

Wollschläger, U., & Roth, K. (2005). Estimation of temporal changes of volumetric soil water content from ground-penetrating radar reflections. *Subsurface Sensing Technologies and Applications*, *6*(2), 207–218. https://doi.org/10.1007/s11220-005-0007-y

Wu, K., Rodriguez, G. A., Zajc, M., Jacquemin, E., Clément, M., De Coster, A., & Lambot, S. (2019). A new drone-borne GPR for soil moisture mapping. *Remote Sensing of Environment*, *235*, 111456–111458. https://doi.org/10.1016/j.rse.2019.111456

Wu, Y., Guo, L., Cui, X., Chen, J., Cao, X., & Lin, H. (2014). Ground-penetrating radar-based automatic reconstruction of three-dimensional coarse root system architecture. *Plant and Soil*, *383*(1-2), 155–172. https://doi.org/10.1007/s11104-014-2139-0

Xu, L., & Oja, E. (1993). Randomized Hough transform (RHT): Basic mechanisms, algorithms, and complexities. *CVGIP: Image Understanding*, *57*(2), 131–154. https://doi.org/10.1006/ciun.1993.1009

Yan, H., Dong, X., Feng, G., Zhang, S., & Mucciardi, A. (2013). Coarse root spatial distribution determined using a ground-penetrating radar technique in a subtropical evergreen broad-leaved forest, China. *Science China. Life Sciences*, *56*(11), 1038–1046. https://doi.org/10.1007/s11427-013-4560-7

Yang, Y., Wu, J., & Christakos, G. (2015). Prediction of soil heavy metal distribution using spatiotemporal Kriging with trend model. *Ecological Indicators*, *56*, 125–133. https://doi.org/10.1016/J.ECOLIND.2015.03.034

Yiruhan, S. M., Akiyama, T., Wang, S., Yamamura, Y., Hori, Y., & Ailikun (2014). Long-term prediction of grassland production for five temporal patterns of precipitation during the growing season of plants based on a system model in Xilingol, Inner Mongolia, China. *Ecological Modelling*, *291*, 183–192. https://doi.org/10.1016/J.ECOLMODEL.2014.07.018

Zajícová, K., & Chuman, T. (2019). Application of ground penetrating radar methods in soil studies: A review. *Geoderma*, *343*, 116–129. https://doi.org/10.1016/J.GEODERMA.2019.02.024

Zhang, P., & Shao, M. (2015). Spatio-temporal variability of surface soil water content and its influencing factors in a desert area, China. *Hydrological Sciences Journal*, *60*, 96–110. https://doi.org/10.1080/02626667.2013.875178

Zhao, Y., Peth, S., Hallett, P., Wang, X., Giese, M., Gao, Y., et al. (2011). Factors controlling the spatial patterns of soil moisture in a grazed semi-arid steppe investigated by multivariate geostatistics. *Ecohydrology*, *4*, 36–48. https://doi.org/10.1002/eco.121

Zhu, S., Huang, C., Su, Y., & Sato, M. (2014). 3D ground penetrating radar to detect tree roots and estimate root biomass in the field. *Remote Sensing*, *6*, 5754–5773. https://doi.org/10.3390/rs6065754